# Investigation of fracture source mechanisms through full-field imaging and acoustic emission

Raphael Heinzmann, Rian Seghir, Syed Yasir Alam, Julien Réthoré

# Investigation of fracture source mechanisms through full-field imaging and acoustic emission

Raphael Heinzmann[a], Rian Seghir[a], Syed Yasir Alam[a], Julien Réthoré[a]

[a]*Nantes Universite, Ecole Centrale Nantes, CNRS, GeM, UMR 6183, Nantes, F-44000, , France*

**Abstract**

The identification and understanding of fracture processes is a vital component in securing engineering structures. By collecting data through experiments or simulations, the identification of material parameters and the understanding of failure mechanisms can be investigated. In the context of in-laboratory experiments, this is done by provoking fracture process through destructive testing (TD) techniques, while collecting data by non-destructive testing (NDT) techniques and postmortem analysis. While NDT techniques are often used individually, increasing interest is given to collective investigations of source activities. Like this, limitations of one method can be compensated by the next. A multi-modal experimental setup is proposed for holistic understanding of failure mechanisms. Combined time resolved AE, DIC and in-volume measurements with post-mortem fracture surface analysis are applied on PMMA tensile cracking experiments for the purpose of AE localization, crack tip detection and determination of crack front complexities and kinematics, respectively. Both high and lower amplitude AE signals were captured and respectively associated to localized dynamic instabilities and stable crack advance. Signals are analysed individually using localization, waveform analysis, and AE descriptor classification. Crack front velocity heterogeneities are identified as valuable quantity to correlate with fracture induced AE responses. For dynamic instabilities, a linear relationship between AE absolute energy and crack propagation area was found. While identification and analyses of local and global dynamic instabilities has shown to be rather trivial, difficulties arose with respect to quasi-static related AE events.

*Keywords:* Polymers, Fracture Mechanics, DIC, AE, Source Localization

## 1. Introduction

To improve the security of engineering structures, one needs to identify and understand different failure sources. The understanding of fracture behaviours, their initiation and propagation, is vital in the field of mechanical engineering. With the aim of collecting experimental data to support the understanding through simulations, different fracture processes are provoked in laboratories by destructive testing (DT) techniques (e.g. fatigue, tensile (elongation) or torsion experiments), with non-destructive testing (NDT) techniques monitoring the activity. Classical experimental setups present an individual application of NDT methods for data collection. However, combining different NDT methods can provide a more robust and adequate understanding of the phenomenon of interest, due to the particular set of advantages and limitations of each NDT technique (Wang et al., 2020; Kong et al., 2020).

One commonly used technique is the method of Acoustic Emissions (AE). With the material being subjected to external loads, sudden stress redistribution take place in the material due to permanent or irreversible damage phenomena. This causes the release of elastic strain energy in the form of dissipated heat and elastic waves. The transient elastic waves, as surface motion, are captured by a transducer translating the mechanical to electrical energy through the process of piezoelectricity (Arnau and Soares, 2008). After preamplification, electrical signals are interpreted and used for the investigation of source activities. Globally, AE analysis can be subdivided into three branches of application: localization, lifetime prediction and damage analysis. The aim of this work is however solely related to AE as a technique for damage analysis, where AE signals have shown to be highly dependent on the type of source mechanism. Different physical or chemical phenomena – material degradation (e.g. cracking (Kong et al., 2020)), reversible processes (e.g. melting or solidification (Wadley and Mehrabian, 1984)), fabrication processes (e.g. grinding (Jayakumar et al., 2005)), leak and flow (e.g. gas evolution (Cao et al., 1998)) – have been identified in literature as potential AE source mechanisms. The appearance of these source activities are generally identified – supported by methods like machine learning (Almeida et al., 2023; Ciaburro and Iannace, 2022), parameter clustering analysis (Li et al., 2014) or waveform processing analysis (Arumugam et al., 2011) – through the identification of similar waveform characteristics of repetitive signals. However, the complexity around accurate interpretation of the AE activity by the user prevails in each considered method. Hence, to support the process of interpretation of AE signals, it seems useful to approach AE analysis through the scope of reverse engineering. Due to direct visible access to the fingerprint of the source activity on the fracture

surface, cracking phenomena seem to present a suitable activity of interest for such investigation. The complete picture of the link between AE activities, state variables, fracture mechanisms and fingerprints on the post-mortem fracture surface might provide valuable information for the design of robust and reliable NDT algorithms.

To achieve a holistic understanding of source mechanisms during fracture experiments of classical quasi-fragile material, this work proposes a multimodal experimental setup combining different NDT tools. With the purpose of AE localization, crack tip detection and determination of crack front complexities, combined time resolved AE, DIC and in-volume measurements with post-mortem fracture surface analysis are applied on cracking experiments, respectively. Each technique was considered to bypass the need of blind interpretation, while allowing to tie AE signals to fracture surface patterns, i.e. enabling traceability of any captured AE signal to the spatial position of the elastic waveform formation on the fracture surface. Model experiments on PMMA are performed under predominant mode I loading conditions leading to stable crack propagation, where heterogeneous crack fronts generate high density of AE emissions with localized dynamic instabilities, that are leading to high amplitude AE responses. Compared with proper pure mode I experiments as a baseline and unstable alternate (stick-slip) cracking (previously investigated in (Heinzmann et al., 2023), the paper discusses the complexity around the ability of correlating AE to local fracture regimes. Such experiments may help the chain of understanding the connection of fracture mechanisms and their AE signature.

The presented work is structured as following: at first, the experimental setup is described by giving detailed information on the applied NDT methods DIC, AE and crack front extraction. Thereupon, a metrological assessment of AE source localization and DIC crack tip detection is presented to verify the applicability of the established inverse problem and detection of the equivalent elastic crack tip position w.r.t. complex crack fronts, respectively. The presented work is then concluded by a discussion on the PMMA fracturing through the multi-point view setup.

## 2. Experimental program

### *2.1. Material, sample geometry and AE sensor placement*

TDCB-shaped samples were obtained from 8 mm thick molded PMMA plates (Plexiglas®) through laser cutting (Class-4 laser system). To make intended in-volume recordings possible, only transparent PMMA plates were considered. The sample geometry, as well as AE sensor positions are shown

in Figure 1. The coordinates $(x; y)$ of the sensor positions, with the notch tip as origin, are marked in red.

Two types of macroscopically stable crack propagation tests have been performed:

a) Smooth quasi-static mode I crack propagation. Pin holes were drilled manually to ensure perfect perpendicularity between pine hole axis and sample face.

b) Same test as the first, however, the pin holes were machine drilled with laser cutting. Here, clearance angles in the pin holes induces transverse loads constraining the crack. The combination of normal axial loads with supplementary transverse loads provoked cracking with a rough crack profile and relatively intense AE activity.

With the objective of this work being the investigation of AE and crack growths relationship, the second case has been considered to be a good candidate with the pure mode I crack propagation case serving as reference. In the continuation of the work, this type of cracking will be referred to as complex, while referring to the reference case as smooth. For discussion, the presented data is combined with AE measurements from previous experiments (Heinzmann et al., 2023), where unstable crack propagation where analysed though the eye of linear elastic fracture mechanics (LEFM) theory, without presenting the AE measurements.

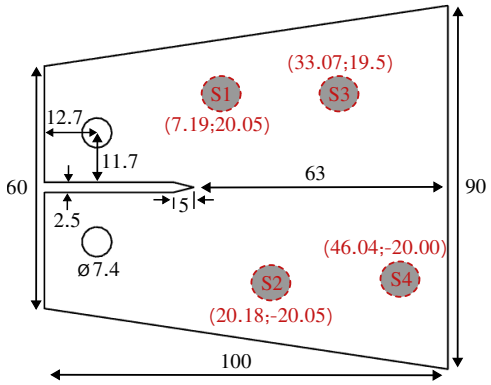


Figure 1: Sample geometry with the AE sensor positions and their coordinates (red) with respect to the notch tip [mm]. Radius of the notch tip is defined by the laser beam diameter of approximately 200 $\mu$m.

Table 1: List of experiments.

| Test | Cracking type |
|---|---|
| Reference | Purely mode I (smooth) |
| T5, T13 | Predominantly mode I with bending (complex) |

### *2.2. Loading and test configuration*

Experiments were conducted with an ElectroPuls E10 000 Instron device with a load cell of 1 kN maximum loading capacity. The room temperature was controlled at 21°C. With a two staged loading procedure (Heinzmann et al., 2023), influences of the notch tip on the cracking process were avoided. Extension rates of 0.01 $mm.s^{-1}$ were applied during the first loading stage initiating an approx. 1 cm pre-crack, while subsequent cracking was driven by extension rates of 0.07 $mm.s^{-1}$.

### *2.3. Experimental setup and methods*

The investigated crack propagation was simultaneously monitored by an AE sytem (MISTRAS Express-8) and a camera system with two high-resolution cameras (Viework VP-50MX-M/C 30). Each of the cameras, having different purposes, faced one side of the sample. One camera was used to perform DIC, while the other was used for in-volume fracture surface recordings of the propagating crack. This was achieved by placing the camera with an inclination towards the sample surface. Notice that in-place alignment has been checked to make face-to-face image registration straightforward. Lightning for the cameras was provided by multiple EFFI-Sharp PWR FF (Effilux) LED projectors. The sample surface facing the camera intended for DIC measurements was coated with a speckle pattern. A form was designed and attached to the surface before coating the surface with regular spray paint, in order to ensure the best AE sensor to surface coupling by protecting the intended sensor positions from paint. Furthermore, consistent sensor placement from one test to the other was eventually achieved. Four AE sensors, positioned as visualized in Figure 1, were used to capture AE activities. To improve AE localization, sensors were placed with horizontal offsets. Synchronous triggering of the systems was performed with a trigger box (R&D vision) being activated by the stage change of the Instron device. Like this, temporal accordance of the devices was achieved to simplify data comparison in the wake. A sketch of the experimental setup with a picture of a mounted sample is presented in Figure 2, while camera hardware parameters are given in Table 2.

Table 2: Camera hardware parameters

| Purpose | DIC | In-volume |
|---|---|---|
| Camera | Viework VP-50MX-M/C 30 | |
| Image resolution | 7856 × 1300 pix | |
| Acquisition rate | 62.5 fps | |
| Lens | TOKINA 100 mm | |
| Aperture | f/2.8 | |
| Field of view | 37.18×6.15 mm | 49.75×8.23 mm |
| Resolution | 4.65 $\mu$m | 6.17 $\mu$m |
| Patterning technique | Spray paint | |

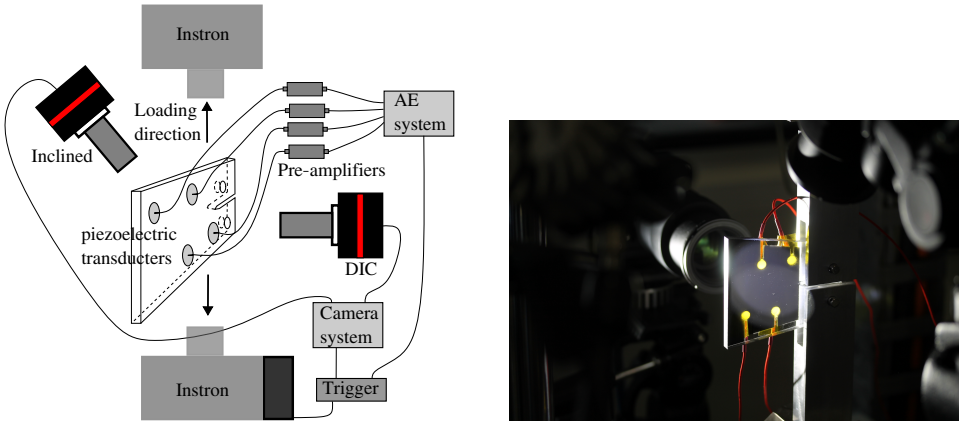


Figure 2: (a) Sketch of the experimental setup and (b) picture of an unbroken sample mounted in the mechanical device.

### *2.4. Digital image correlation (DIC)*

By taking sequential images of the deforming sample, displacement fields can be obtained using DIC. It is based on the principle of conservation of brightness between reference ($f$) and deformed images ($g$) (equation of optical flow). This ill-posed non-linear inverse problem has the following form:

$$f(\underline{X}) = g(\underline{X} + \underline{u}(\underline{X})) \tag{1}$$

where $\underline{u}(\underline{X})$ presents the sought displacement field. The following ill-posed non-linear problem is eventually solved iteratively (Quasi-Newton method)

using FE-based quadrilateral elements and bi-linear shape functions. Furthermore, with the displacement field obtained through DIC and a post-projection of the displacement field onto the Williams' series expansion, fracture parameter can be derived (Roux and Hild, 2006; Réthoré, 2015). Among others, the method allows for the detection of the crack tip position with a sub-pixel accuracy. For more details on the extraction of fracture mechanics parameters, the authors refer to the Appendix A presenting an extraction from (Heinzmann et al., 2023). DIC and Williams' series projection has been performed by using the library of the open-source software UFreckles (Réthoré, 2018), while required variables are listed in Table 3. Notice that in the context of this work only crack tip position will be analysed, with the projection zone ($R_{min}$ and $R_{max}$) being defined by a parametric study. Furthermore, with DIC techniques working in pixels, a conversion variable is needed to find the corresponding metric/imperial data. Taking an image of a ruler placed on the sample surface and using an FFT analysis, the pixel to meter conversion value is systematically obtained with a sub-pixel precision. Finally, a Savitzky-Golay filter (Polynomial), with a rolling windows of 50 ms, i.e. 3 frames, is applied on projected data.

Table 3: DIC & Williams' series parameters

| DIC | |
|---|---|
| Software | UFreckles (Réthoré, 2018) |
| Discretization | FE-based global DIC |
| Shape function | Bi-linear quadrilateral Lagrange element (Q4P1) |
| Element size | 95 $\mu$m |
| Post-filtering | Median filter using $1^{st}$ neighbour applied to U |
| Williams' series projection | |
| E | 3.5 GPa |
| $\nu$ | 0.32 |
| $R_{min}$ | 127.8 $\mu$m |
| $R_{max}$ | 1301.6 $\mu$m |
| 2D approximation | Plane-stress |

### *2.5. Acoustic emission(AE)*

AE analysis was performed with four resonant piezoelectric sensors (Medium Frequency resonant Miniature sensors Nano30 by MISTRAS). They have been mounted with conductive scotch and super glue. AE data was ob-

tained by the AEwin streaming option to improve optimal recovery of AE activity by taking advantage of the short experiment duration (5 s). Hence, signal descriptors and waveforms were computed, through in-house Matlab scripts during post-processing. The AE responses were enhanced by a pre-amplifier with a gain of 40 dB, while background noise filtering through an imposed threshold was unnecessary since AE data was retrieved by streaming. The system was calibrated and tested for appropriate coupling before each test through the pencil lead break procedure (Scruby, 1987).

### *2.6. Crack front identification*

Collecting information from within the volume, one would need CT scan techniques (Crandall et al., 2017) for the investigation of opaque materials. However, with PMMA existing as transparent material, capturing crack front kinematics is feasible with standard imagine techniques. To do so, the camera system has to be placed with an inclination to the sample surface causing experimental challenges in providing sufficient light and sharpness over the full sample length and thickness. Thus, lens and light settings were defined on a test sample, in which the crack propagated to about half of the sample length. However, already tiny deviations from the crack path of this example case led to strong local variations and losses in sharpness and light with respect to each newly propagating crack. Hence, a compromised lens setting and light positions had to be used to facilitate the recovery of the crack front kinematics for any possible crack path. For post-processing, a crack front extraction algorithm was built along the following steps:

1. *Normalization:* To begin with, images were normalized to correct for light variations between frames.

2. *ZOI:* A zone of interest (ZOI) around the crack front was defined, within which the extraction was performed.

3. *Revealing advancement:* To reveal the advance of the crack front, preceding images were subtracted from the current one. To increase robustness, not only one preceding image, but the average of a pre-defined number of preceding images was taken into consideration.

4. *Binarization:* A pixel threshold, based on the mean and standard deviation (std) of the newly created image (step 3), was defined. This threshold was used to binarize the image.

5. *Erosion and dilation:* The binary image was eroded (to remove unwanted pixels) and dilated (to recover continuous objects).

6. *Boundary:* Tracing the boundaries of each object to define their pixel coordinates by the MATLAB function bwboundaries, which is based on the Moore-Neighbor tracing algorithm modified by Jacob's stopping criteria (Gonzalez et al., 2004).

7. *Exclusion:* Excluding tiny objects with a minimum amount associated pixels.

8. *Reconstruction:* Rebuilding the crack front mask based on the different objects.

9. *Finishing:* Recovering a clean crack front by only considering the most advanced position of the rough crack front mask.

10. *Smoothing:* Applying a moving median filter to reduce periodic trends from outliers along the crack front.

It is worthwhile mentioning that the difficulties in recording sharp images of the in-volume crack propagation resulted in the algorithm partially not being able to clearly identify and extract the crack front. This is particular prominent along the edges of the crack front.

## 3. Metrological assessment of crack tip detection and AE localization

### *3.1. Assessment of AE source localization*

#### *3.1.1. Methodology*

The method of AE source localization is a widespread addition to standard AE analysis. With the use of multiple AE transducers, depending of the intended dimension of observation, AE localization can provide information on the origin of an AE signal. While the accurate definition of wave velocity is key to the precision of traditional methods of AE source localization (e.g. (Schmidt, 1972; Schau and Robinson, 1987; Abel and Smith, 1987; Romhány et al., 2017; Zhou et al., 2018)), recent studies focus on the development of wave velocity independent AE source localization methods (e.g. (Ciampa and Meo, 2010; Dehghan Niri and Salamone, 2012; Dong et al., 2019)). A review focusing on sensor quantity, investigated structural geometries and method performance of the different existing localization techniques is presented in Hassan et al. (Hassan et al., 2021).

For the presented work, an inverse problem for AE source localization – treating wave velocity as unknown – is proposed using four AE transducers. While this problem presents itself as ill-posed (Zhou et al., 2021), it can easily be

build for multiple sensors (here, $n = 4$). Based on proportional relationships of distances and travel times between source and sensors, 2D source coordinates can be expressed by the nonlinear governing equation, with the assumed AE source location $(x_s, y_s)$ and sensor positions $(x_i, y_i)$ for all i from 1 to $n$. The equation is taking the following form:

$$(x_i - x_s)^2 + (y_i - y_s)^2 - v^2(t_i - t_s)^2 = 0, \quad \forall i \in [1, n] \tag{2}$$

where $t_i$ and $t_s$ are the arrival time of the signal at each sensor and the time the signal has been released at the source, respectively. To linearize such nonlinear and coupled equation, variables $x_s$, $y_s$, $t_s$ and $v$ are substituted, respectively, by $x_o + \mathrm{dx}$, $y_o + \mathrm{dy}$, $t_o + \mathrm{dt}$, and $v_o + \mathrm{dv}$. These linearized contributions of Equation 2 then take the following form:

$$(x_i - x_s)^2 = (x_i - x_o)^2 + 2\mathrm{dx}(x_i - x_o) + \mathrm{dx}^2 \tag{3}$$

$$(y_i - y_s)^2 = (y_i - y_o)^2 + 2\mathrm{dy}(y_i - y_o) + \mathrm{dy}^2 \tag{4}$$

$$-v^2(t_i - t_s)^2 = -(v_o^2 + 2\mathrm{dv}v_o + \mathrm{dv}^2)[(t_i - t_o)^2 + 2\mathrm{dt}(t_i - t_o) + \mathrm{dt}^2] \tag{5}$$

where $x_o$, $y_o$, $t_o$ and $v_o$ are the initial guesses with the current increments dx, dy, dt and dv.
After neglecting squared and weakly coupled terms, Equation 2 extended by Equations 3, 4 and 5 leads to a four equation four unknown linear system.

$$L = 2\begin{bmatrix} x_i - x_o & y_i - y_o & -v_o^2(t_i - t_o) & v_o(t_i - t_o)^2 \end{bmatrix} \tag{6}$$

$$b = \begin{bmatrix} (x_i - x_o)^2 + (y_i - y_o)^2 - v_o^2(t_i - t_o)^2 \end{bmatrix} \tag{7}$$

The system is eventually solved in a least squares minimization process as following:

$$L^\intercal L = L^\intercal b \tag{8}$$

*3.1.2. Uncertainty*

To evaluate the performance of the AE source detection and identify possible weak spots in the method, localization has been performed on synthetic AE signals. To mimic the localization of AE signals, time of arrivals (TOA) of the synthetic AE signals for all four sensors had to be computed. For this, the following elements were considered:

- Young's modulus (E) = 3.5 GPa
- Material density ($\rho$) = 1200 kg.m$^{-3}$

- Velocity (v) $= \sqrt{E/\rho} = 1707.8$ m.s$^{-1}$
- Distance to the sensors $i$ $(d_i) = \sqrt{(x_i - x_s)^2 + (y_i - y_s)^2}$, with $(x_i, y_i)$ and $(x_s, y_s)$ being the sensor and source coordinates, respectively.
- Time of arrival $(\mathrm{TOA}_i) = d/v$

In the following, (a) the influence of the initial guess position on the localization uncertainty for various random source position and (b) the influence of synthetic AE signals corrupted by expected experimental biases are investigated.

Firstly, the non-linear problem is highly sensitive to the initial guess. To highlight this sensitivity, localization error due to the initial guess has been mapped for various random source positions. For each random position of AE source, the AE localization was performed for a grid of 50x50 initial guesses. As illustration, the initial guess error map is presented in Figure 3 for four random AE source positions. $\sigma$ denotes the distance between the located source position and its real location. The figure reveals that for some initial guess (yellow areas), the algorithm may not only poorly converge but even diverge which highlights the strong initial guess dependency. In practice, the cost function is not always convex depending on the source location, so no convergence may be achieved leading to areas of 'forbidden' initial guesses. Furthermore, no particular initial guess area leading to good localization ($\sigma$ =∼1 mm) for any potential source position was detected within the field of interest. Hence, an evaluation to find the most suiting initial guess has to be performed before each source localization run, i.e. any new sought for AE signal requires its own optimal initial guess identification. This can easily be achieved a priori knowing the crack tip position from DIC and using the proposed numerical twin being presented in this section.

Secondly, to shift the model scenario closer to a real case, main order experimental biases are introduced to the process of localization. A random normal distributed error was drawn and appropriately scaled for each term of interest. The target term with their standard deviation of the imposed uncertainty can be found in Table 4. The potential errors for sensor placement, TOA and velocity were determined with respect to AE transducer radii of 3.7 mm, AE temporal resolution of 0.1 $\mu$s and expected wave speeds of 1707.8 m.s$^{-1}$, respectively. It is worthwhile mentioning that the TOA has been identified as the most critical variable for a successful AE source localization. A rather large uncertainty was thus introduced here (about 10 times the AE sampling) to stress-test the algorithm. Indeed, signals need on average 10 $\mu$s to propagate through the field of

view presenting, on average, a signal to noise ratio of 90% on the TOA. However, when the source goes closer to one of the sensors, since the uncertainty is kept at 1 $\mu$s, the signal to noise ratio decreases a lot with the propagation time going closer to the uncertainty floor. Furthermore, identification of the TOA through cross-correlating waveforms – to achieve sub-resolution accuracies – was not possible with waveform characteristics changing from one sensor to the other (see Appendix C). While regular threshold crossing and floating threshold crossing are the most basic methods of TOA detection, more advanced methods are proposed in literature. Cheng et al. (Cheng et al., 2021) compared such methods in the case of I-shaped steel girder. With large differences in peak amplitude, the TOA was determined in the presented work through a dynamic threshold and verified by the Akaike Information Criterion (AIC) method (Hensman et al., 2010). The dynamic threshold was defined as twice the standard deviation of the absolute volt amplitude. It was additionally possible to control and potentially adapt the TOA, due to the rather manageable amount of AE hits.

Table 4: Standard deviation (uncertainty) added to synthetic source position, time of arrival and first guess of velocity.

| Error | Standard deviation |
|---|---|
| Sensor position | 500 $\mu$m |
| TOA | 1 $\mu$s |
| Velocity | 5 m.s$^{-1}$ |

Various AE source locations were tested to evaluate the performance of the localization algorithm with respect to different areas of the field of interest. Figure 4 is showing the uncertainty (in $x$ and $y$ direction) of the source localizations spanning a 20×20 grid. Each localization is presented as the median absolute deviation (MAD) of the 200 iterations with changing copies of noise. A priori identified optimal initial guesses however were kept constant for all 200 runs. Highest uncertainties (MAD around 20 mm) for the localization are shown in yellow, while good identification of the source (MAD below 1 mm) are shown in dark blue. With higher accuracies in the vicinity of the barycenter of the four sensors, two main areas of weak performance can be observed below sensor one and above sensor four. Hence, with the localization accuracy showing strong local variations, uncertainties have to be evaluated independently for each localization attempt.

Ultimately, the evaluation of uncertainties shows that localization of experimental AE signals will need to consist out of the evaluation of the best suiting

initial guess and the area dependent localization uncertainty. The later will be indicated by an error envelope (red dashed ellipse) around the detected source position for any detected AE signal. In the context of this work, due to the inferior spatial localization accuracy, AE localization does not compete against DIC crack tip detection, but as support to verify the link between the propagating crack and the AE activity. With no a priori existing proof that AE signals are actually emitted by the creeping crack, one needs to account for the risk of linking potential noise signals to the crack. Moreover, it is worthwhile mentioning that, considering through thickness variation of the crack front ($\pm 600\mu$m), the 2D AE localization will not provide valuable information for discriminating from which part of the front the AE has been emitted. However, sensibility of the method to in-volume variations has still been evaluated (not presented here), showing no particular additional bias on in-plane localization, other than on the velocity identification.

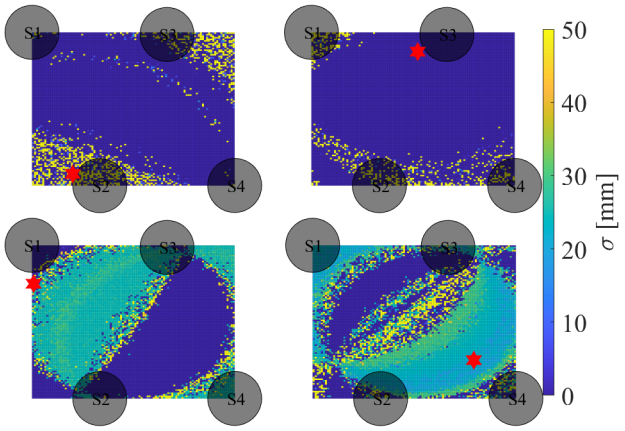


Figure 3: Map representing the sensitivity of the initial guess (50×50 grid) on the localization error for four random of AE source positions. $\sigma$ denotes the distance between the located source position and its real location (red star). Sensors are presented in scale of the real sensor base area with the area of interest being approx. 40 × 40 mm (see Figure 1)

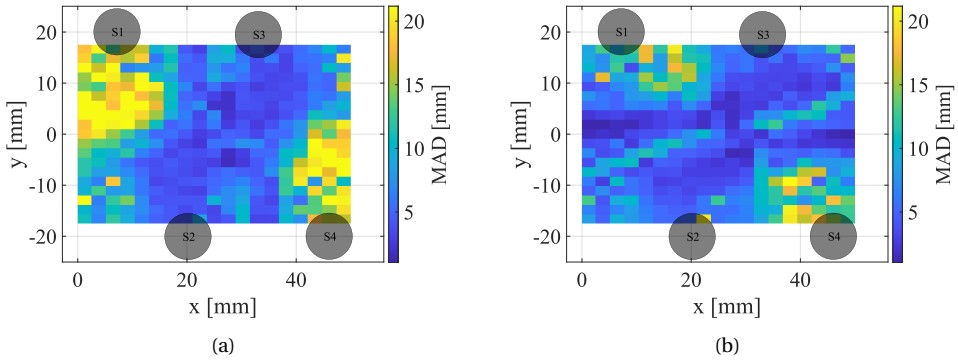


Figure 4: Median absolute deviation (MAD), i.e. mean identification uncertainty discarding outliers, on source localization depending on the source position (20×20 grid) for (a) x-direction and (b) y-direction. Sensors are presented in scale of the real sensor base area.

### *3.2. Assessment of crack tip detection from DIC*

In literature, using DIC displacement fields and Williams' series expansion has become a classical method for the identification of the crack tip position (Hamam et al., 2007; Roux et al., 2009; Henninger et al., 2010; Réthoré and Estevez, 2013; Réthoré, 2015; Roux-Langlois et al., 2015). However, while a numerical investigation with a curved crack front in (Réthoré et al., 2011) estimated the apparent elastic crack tip position systematically in front of its free surface appearance, it has not been explored experimentally. Here, we have tried to elucidate this question through in-volume recordings of transparent PMMA plates with the back-face inclined camera. Thanks to temporal synchronization of the devices, each DIC frame had a corresponding in-depth image visualizing the crack surface at this time. By taking the pixel to meter conversion values of the two cameras into account, spatial matching was performed by taking the notch tip as common reference point. Like this, as presented in Figure 5, detected crack tip positions were found in the in-depth visualizations of the fracture surface. Here, the crack tip detection on the DIC side and within the in-volume images are presented for the first ((a) and (c)) and last ((b) and (d)) frame of experiment T13, respectively. The white rectangle in Figure 5(a) and (b) is showing the field of view (FOV) of the DIC process. In Figure 5(c) and (d), the DIC face is found on the upper side of the fracture surface, with the red dashed line indicating the the crack tip position detected by DIC through the thickness of the sample and the crack front highlighted in green retrieved by the crack front extraction algorithm (see Section 2.6). By taking the constant uncertainty on the determination of the notch position in the images (approx. 20 pix) and on the pixel to meter conversion ratio from the

FFT analysis (approx. $1.27\times10^{-4}$) into account, the global uncertainty on the DIC crack tip detection has been found to be not more than 45 $\mu$m (see (Heinzmann et al., 2023) for details). By taking all the above into consideration, the following points can be observed:

- Evaluated uncertainties are lower than the in-depth crack front variations.
- Despite the in-depth crack front complexity, the crack tip is systematically detected at the position of the crack front on the DIC face.

Hence, DIC-based estimation of the crack tip position is suggested to be the estimation of the crack tip at the surface and not an in-depth average. The presented experiment, with a highly heterogeneous crack front made of multiple ligaments progressing and nucleating at different rates shown by bright white lines in Figure 5(c) and (d), eventually shows that DIC-based crack tip detection does not fully render such in-volume complexities.

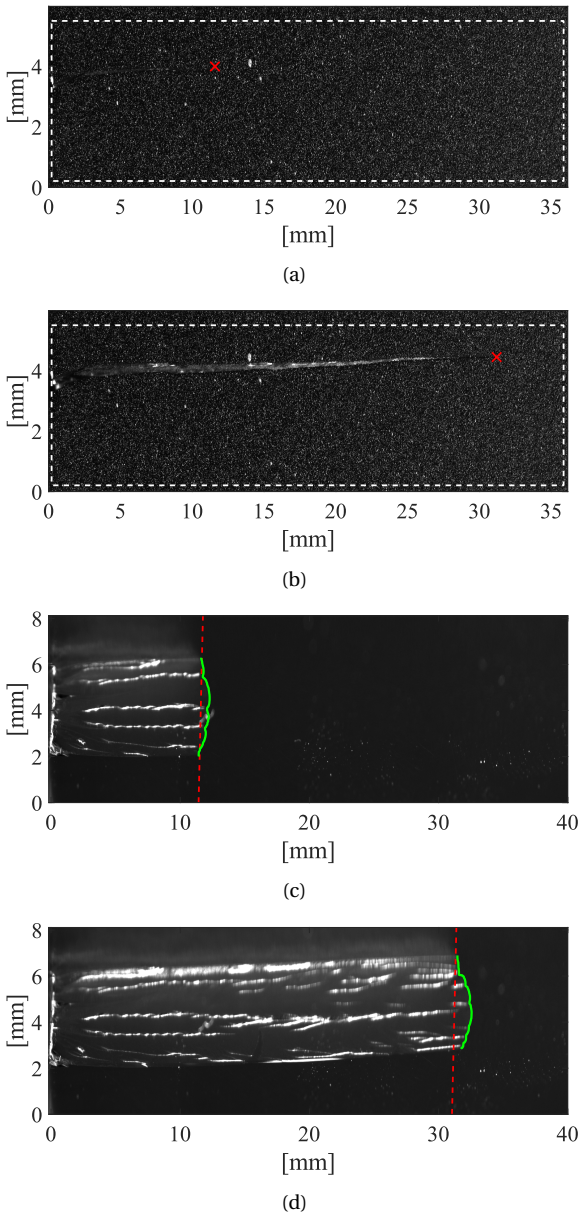


Figure 5: Accuracy in crack tip detection by Williams' series for first ((a) and (c)) and last ((b) and (d)) frame of the experiment T13. (a) and (b) shows the crack tip detection on the DIC face, with the white rectangle marking the FOV. (c) and (d) is showing the in-volume recording, where the DIC crack tip detection is vertically prolonged from the surface equivalent elastic crack tip position by the dashed red line and the crack front (obtained by the crack front extraction algorithm) is highlighted in green. The DIC face is found at the upper side of the crack surface in (c) and (d), while the maximal potential uncertainty in the equivalent crack tip detection related to the two frames is found to be approx. 40 and 45 $\mu$m, respectively.

## 4. Results

Fracturing of TDCB shaped PMMA samples were investigated through DIC, in-volume recordings, microscopy and AE. The time of interest for each experiment was 5 seconds during which, based on a common trigger (see Section 2), all time-dependent devices recorded simultaneously. Microscopic images of the fracture surface were obtained by a numeric microscope (Keyence) with a spatial resolution of 2.53 $\mu$m/pix. With DIC being a surface measurement tool, images obtained by the inclined camera provide in-volume understandings of crack front complexities to account for deviations of the crack tip location measured on the DIC face to the crack front within the volume. Eventually, AE localization is performed to confirm that AE signals are actually emitted within the vicinity of the crack front and thereby avoid any misconceptions by potential environmental noise. DIC displacement fields and their corresponding Williams' series projections are presented in Figure 6.

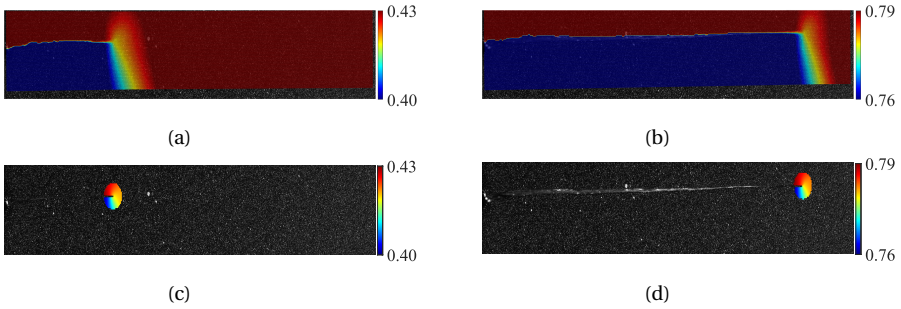


Figure 6: Vertical displacement field [mm] and corresponding Williams' series projection [mm] within the domain surrounding the crack-tip (defined by $R_{min}$ and $R_{max}$) of the first and last recorded image for experiment T13. The used Williams' series parameters are listed in Table 3.

### *4.1. Distinctive macroscopic features of the cracking cases*

As introduced earlier, two propagation scenarios – a reference (smooth model crack propagation) and two complex cracking experiments (closer to real case life cracking scenario) – have been investigated from surface kinematics and acoustic emissions points of view. More precisely, a pure mode I fracture experiment is denoted as reference, with T5 and T13 presenting complex fracturing experiments. Let us start from a macroscopic perspective. By presenting the three experiments in the space of normalized crack length as a function of experimental time (Figure 7(a)) and velocity as a function of the normalized crack length (Figure 7(b)), their difference in cracking behavior is highlighted. The normalization of the crack length is done with respect to the

maximal possible crack propagation distance of 63 mm, imposed by the sample geometry (Figure 1). The crack propagation of the first loading stage, i.e. pre-crack, is leading to slightly (±3 mm) different starting positions of the crack length for each experiment. Apart from really tiny steps in T5 (at 2.4 s, 3.2 s and 4.2 s) and T13 (at 2.25 s and 3.0 s), crack propagation differences are almost unrecognizable in the three cracking cases by focusing on the crack length evolution. However, by taking velocities into consideration, disturbed propagation of the complex cracking cases becomes more prominent. With an imposed extension rate of 0.07 mm.s$^{-1}$, mean velocities of 4.6 mm.s$^{-1}$, 3.9 mm.s$^{-1}$ and 4.2 mm.s$^{-1}$ are measured for the reference, T5 and T13, respectively. While rather tiny velocity oscillations (±0.5 mm.s$^{-1}$) are found in the reference experiment, strong variations – reaching peak crack speeds of 20-30 mm.s$^{-1}$ – are detected during experiments T5 (±3.9 mm.s$^{-1}$) and T13 (±3.2 mm.s$^{-1}$). Differences in crack behavior become further evident by taking the AE streaming data into consideration. Figure 8 is showing the unprocessed AE streaming output for all three experiments. Only limited AE activity is detected during the reference case experiment, which suggests that elastic waves, potentially released during this cracking, are below the experimental sensitivity of the AE sensors. For the presented results, the average noise level is found to be 3.5 mV (31 dB) for all experiments. However, no clear link between the AE activity along the test and the velocity variations of the complex cracking is found at this stage.

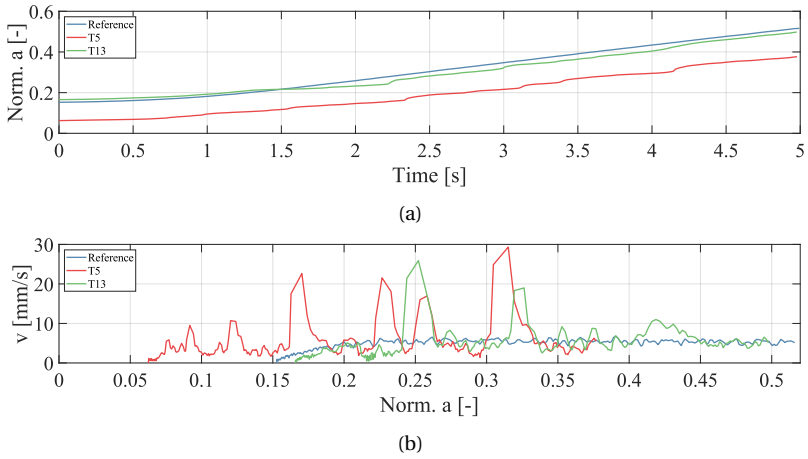


Figure 7: (a) Normalized crack length [mm] as a function of recorded time [s] and (b) velocity [mm/s] as a function of the normalized crack length [mm].

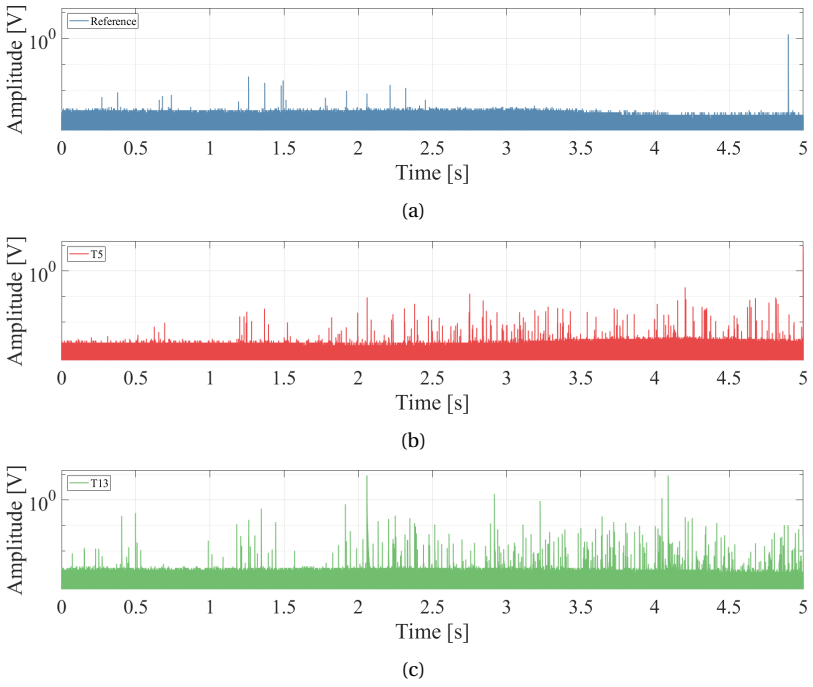


Figure 8: Raw AE streaming data (Amplitude [V] in log-scale vs. Streaming time [s]) of experiments (a) Reference, (b) T5 and (c) T13.

### *4.2. Investigation of complex cracking cases*

Firstly, AE data will be investigated independently by cropping AE waveforms from the streaming and the subsequent computation of AE parameters from those waveforms. By solely looking at the AE streaming output of experiments T5 and T13, strongly differing signals can already be identified within the set of AE responses. With peak amplitudes almost reaching 10 V (100 dB), these signals present a great variation to the average peak amplitude of approx 0.01 V (40 dB) found for all other signals. To understand and identify their origin, we will focus on experiment T13, where two signals (at 2.1 s and 4.1 s) with a peak amplitude of 10 V are detected. To help analyse and classify the AE activity during this experiment, a Principle Component Analysis (PCA) – by taking all AE descriptors into consideration except Time and Threshold – has been performed on the entire set of recovered AE signals (see Appendix B for detailed information on the procedure). Underlining the discrepancy, Figure 9 is showing both high amplitude (HA) signals in comparison with an example waveform of the lower amplitude (LA) signals, and the entire set of signals being presented in the space of the most dominant principle component axis and

their AE descriptor contributions. While the differences in waveform characteristics are easily visible by comparing the two HA signals to the example of a LA signal, it is worthwhile mentioning that similarities comparing the two HA signals are found to be rather small. This becomes further evident by comparing all signals in the space of principle component axis. Indeed, three signals are found to be relatively far from the main cluster of signals that cover the space from approx. -5 to 5 along PC1 and PC2. Among these these signals, the two pre-defined high amplitude signal are the ones deviating the most from the rest presenting a local instability, where its origin is investigated in detail in the following section. However, with only a peak amplitude of 1 V, the third one (appearing at approx. 4.1 s shortly before the second HA signal) deviates from the majority of the lower amplitude signals, but does not compare to the HA signals being associated with local instabilities.

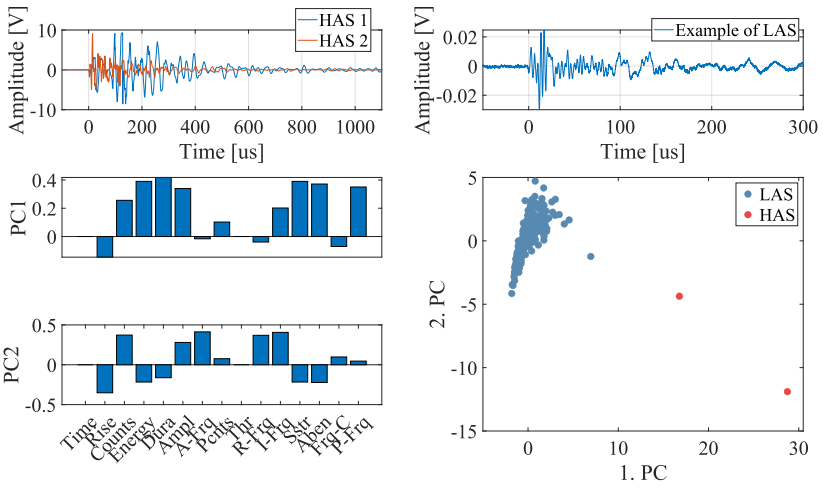


Figure 9: HA signals and an example of a LA signal, contributions to the two most dominant principle component axis (PC1 and PC2) and all AE signals presented in the space of first and second principle component.

### *4.2.1. High amplitude (HA) signals*

To identify the origin of the HA signals, the position of their potential source activity needs to be spatially located on the fracture surface. As previously discussed, the time of arrival of these signals can be associated to a frame of the DIC and inclined recording due to the device synchronization. Considering a camera temporal sampling of 16 ms and wave propagation times (from sensor to any potential source location) below 30 $\mu$s, DIC and AE timelines can be matched without any shift correction. Hence, through means of DIC crack tip

detection and in-volume recordings, the position of the crack front at the potential time of elastic wave formation can be identified. This conclusion only holds true if AE signals are actually associated to the position of the DIC crack tip. The crack tip is identified when any AE signal is received by the transducer even in the case that the signal has not been released by the propagating crack. To eliminate this question and avoid any potential misconceptions, AE source localization was performed. Figure 10 shows the AE source localization of the two HA signals. Black crosses indicate the current position of the crack front (identified by DIC) at the time of the first AE threshold crossing. It is worthwhile mentioning that the indicated crack tip position is the DIC crack tip detection and therefore the position on the DIC face. Hence, no crack front complexities – potential variations of ±650 $\mu$m – are taken into account. Green dots present the results of the AE source localization. As references, positions of the AE sensors (S1, S2, S3 and S4) and the field of view (FOV) covered by the DIC camera are presented with black circles and a dashed rectangle, respectively. The dashed red ellipse indicates the identification uncertainty for this specific source location based on our numerical twin (see Section 3.1.2). With both signals being located within the zone of uncertainty, it is confirmed that the AE signals have been emitted from or within close vicinity of the crack tip. Thus, a deeper analysis of the fracture surface in the spatial vicinity of the crack front for the two considered instants can be pursued.

Figure 11 is showing (a) the spatial evolution of the cumulative absolute energy of the AE activity and the crack front at the instant of the two HA signals on the fracture surface, as well as (b) and (c) detail views of the fracture surface. Crack propagation is from left to right with the notch tip at x = 0 mm. Smooth triangular zones, visible in fracture surface zooms (Figure 11 (b) and (c)), are associated to unstable dynamic crack propagation. Macroscopically smoother fracture surfaces are related to cracks propagating at speeds between 36-200 m.s$^{-1}$ (Heinzmann et al., 2023). The recurrence of dynamic and quasi-static crack propagation with their fingerprint on the fracture surface have already been observed in many studies (Ravi-Chandar and Balzano, 1988; Bonamy and Ravi-Chandar, 2003; Hattali et al., 2012; Vasudevan, 2018), and thoroughly investigated in our recent work (Heinzmann et al., 2023). Such dynamic instabilities, i.e. cracks suddenly jumping over significant distances at average speeds of approx. 100 m.s$^{-1}$, might be induced by thermo-visco-elastic effects through rising temperatures at crack tip (Vincent-Dospital et al., 2020). While large scale dynamic instabilities, under purely mode I cracking conditions, can be provoked by particular extension rates due the existence of forbidden crack tip velocity domain for stable crack propagation (see (Heinzmann et al., 2023)), we observe that unsymmetrical through thickness open-

ings of the fracture front can lead to localized dynamic instabilities even at slower extension rates (0.07 mm.s$^{-1}$ instead of >0.5 mm.s$^{-1}$ for large scale instabilities). Indeed, the particular fracture surface markings, associated with such cracking, are found in large scale and in the local scale.

As illustration, Figure 12 shows the raw streaming output with crack length measurements of large scale instabilities during alternate cracking experiment from our previous study (Heinzmann et al., 2023). Here, dynamic crack propagation is defined by AE signals with peak amplitudes of 10 V (100 dB) and vertical jumps in the temporal evolution of the normalized crack length. In comparison to these previous experiments where the instability stretched smoothly along the entire sample thickness, our current experiments present such mechanism localized on the back side facing the inclined camera. To investigate if there is a potential connection between energy released by the crack front in large scale and localized dynamic instabilities, the relationship between AE absolute energy and surface area spanned by the dynamic crack propagation has been analysed. In that context, Figure 13 presents the AE absolute energy of dynamic bursts as a function of the burst area in semi-log scale. Signals of the dynamic bursts observed during experiment T5 and T13 are being supplemented by those recorded during alternate cracking experiments of our previous study (Heinzmann et al., 2023). While cracks released AE absolute energies between $1.5\times10^7$ to $2.0\times10^7$ aJ to overcome areas of approx. 10-130 mm$^2$ during alternate cracking experiments, AE absolute energies of approx. $6\times10^6$, $5\times10^6$ and $2\times10^6$ aJ for areas of 0.34, 0.24 and 0.067 mm$^2$ were found for dynamic bursts during experiments T5 and T13. Figure 13 is hence suggesting a linear relationship between the AE absolute energy and the log of the crack propagation area. Results are presented for one sensor, while no attenuation is expected due to travel small distances. However, it is worthwhile mentioning that the established relationship does not reflect the complete fracture energy. Retrieved data solely relays on the punctual measurement of the AE transducer. Thus, AE absolute energy measurements – computed as the time integral of the squared voltage signal – bear a proportionate and directional bias, while also relaying on the intrinsic transfer (potentially complex) function of the sensor.

Furthermore, through the identification of local instabilities of the crack front, crack velocity measurements can be reevaluated. For this, the crack front was computed for each frame by the crack front extraction algorithm (Section 2.6). Before deriving the temporal evolution of the crack front to obtain the velocities, the crack front displacements were smoothed over time by a second order polynomial Savitzky-Golay filter over a window of three frames. Figure 14 presents, as a function of the recording time, the DIC determined crack tip

speed, the absolute voltage signal of the AE streaming and in-volume determined velocity map of the entire crack front. By comparing Figure 14 (a) and (b), one can observe that the DIC crack speed increase (Figure 14 (a)) at 2.2 s appears, in time, approx. 100 ms after the detection of the local instability in the AE streaming (Figure 14 (b)). This can be explained by the spatial position of the dynamic burst along the depth of the sample. Taking Figure 14(c) into consideration, local dynamic instabilities can be identified as crack front jumps on the inclined camera face at around 16 mm and 27 mm. Hence, the first peak in the DIC crack velocity can not be associated directly to the instability itself, but rather to the crack front catching up belated with the strong local advancement. It is worth mentioning, that the DIC-side velocities retrieved from the crack front kinematics do match the apparent crack tip speed captured by DIC. However, to enhance visualization of local velocity variations, the presented velocity map in Figure 14(c) limited to an upper bound of 15 $mm.s^{-1}$. Thus, velocity peaks around the local instabilities and their secondary impact on the opposite side are saturated. As reference, the peak crack tip speed appearing as secondary effect on the DIC face are found to be roughly 10 $mm.s^{-1}$ lower than directly measured through the in-volume recordings at the spatial position of the instability. Nevertheless, velocities associated to the local instabilities have to be taken with cautious, since sudden and strong velocity variations can not be appropriately captured with the temporal resolution of the camera (16 ms interframe). Hence, it has to be expected that the dynamically related velocity variations are cropped in amplitude. In the vicinity of the second local instability (4.1 seconds), Figure 14 (b) presents a more homogeneous increase in crack front velocity along the sample thickness covering up potential secondary effects on the DIC face. However, while the first local instability (peak velocity of about 34 $mm.s^{-1}$) was not strong enough to provoke a homogeneous increase in crack tip speed along the entire sample thickness, no observable impact by the second one (a peak velocity of about 22 $mm.s^{-1}$) can be expected on the DIC face.

General observations of the crack front kinematics shown in Figure 14(b) present a rather homogeneous crack front speed for about 2 s until the appearance of the first local instability. Thus, it seems that this local instability produces a disturbance of the crack front behaviour resulting in global, periodic accelerations and declarations of the crack front with local velocity variations.

Finally, Figure 15(a) presents, as a function of the recording time, both crack front velocity heterogeneity (computed as the standard deviation ($\sigma$) of the velocity along the crack front at every time) and the AE streaming of experiment T13. A clear correlation can be observed. Apart from some AE activity and tiny velocity variations, the majority of AE activity and velocity variations are found

after the first dynamic instability at 2.1 seconds. Particularly around 2.1, 2.9, 3.5 and 4.1 seconds, good temporal agreement can be observed between the increase in crack front velocity heterogeneity and the density of the AE activity.

Underlining this correlation, Figure 15(b) and (c) present the interframe threshold crossings (counts), i.e. cummulative counts within a window of 16 ms, as a function of the mean and standard deviation of the velocity along the crack front, respectively. The colorbar presents the experimental time. Both figures highlight the crack front disturbance introduced by the first dynamic instability. Figure 15(b) clearly shows a separation of the homogeneous crack front phase with low AE activity (i.e. small number of interframe counts) from the heterogeneous crack front phase with high AE activity (i.e. high number of interframe counts). However, the separation of these phases is not only found in time with the appearance of the local instability as disruption of the balance crack front propagation, but also by a crack front mean velocity ($\bar{v}$) threshold of about 4 mm.s$^{-1}$. With the interframe count as a function of the crack front variations ($\sigma(v)$), Figure 15(c) is presenting a different angle on the correlation defined in Figure 15(a). A more heterogeneous crack front propagation results in a higher density of AE activity. Again, taking the experimental time into consideration, the first dynamic instability is found in the transition between the two phases.

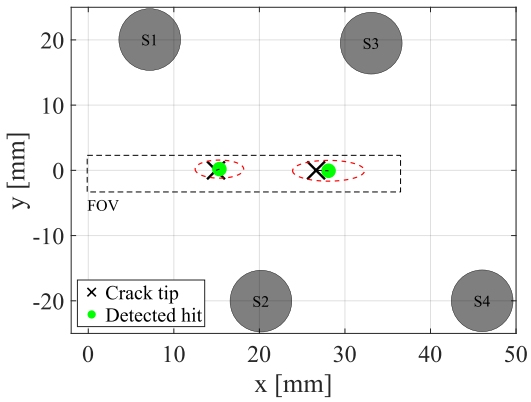


Figure 10: AE localization of the HA signals of experiment T13.

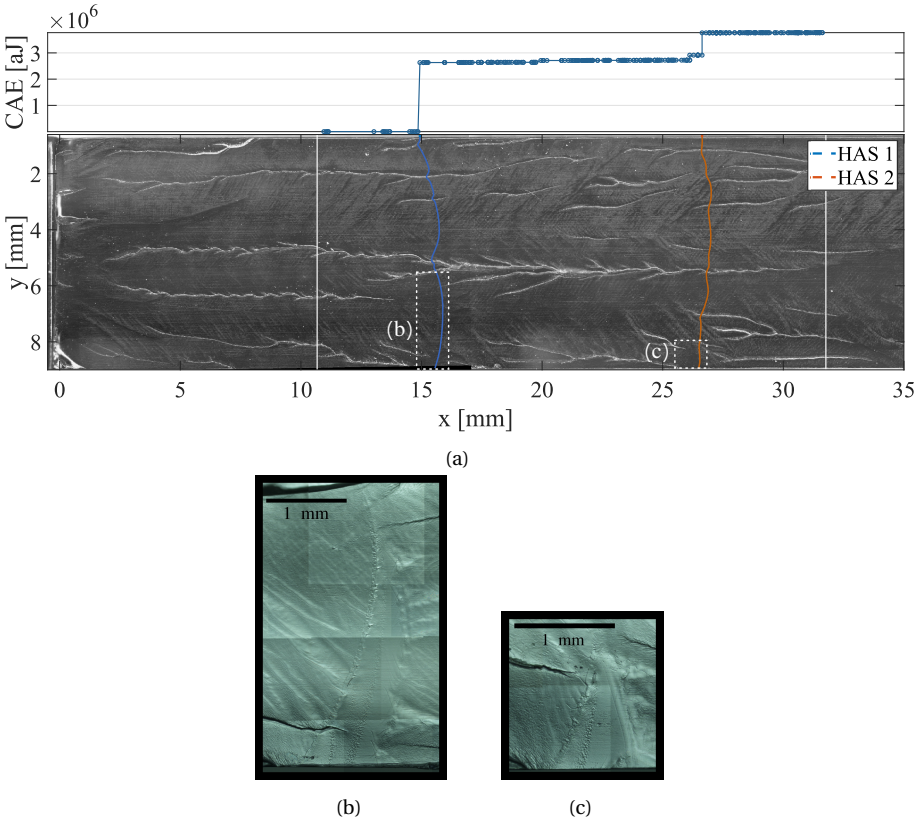


Figure 11: (a) Cumulative absolute energy (CAE) [aJ] of AE signals as a function of the crack tip position on the fracture surface with the crack front complexity for the two signals related to the dynamic bursts. (b) and (c) show a detailed view of the particular fracture surface markings associated to dynamic crack propagation.

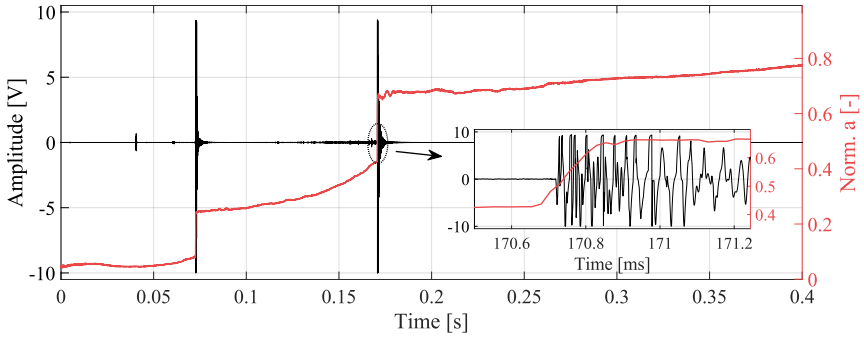


Figure 12: Normalized crack length [-] and amplitude [V] as a function of the recording time for an alternate cracking experiment.

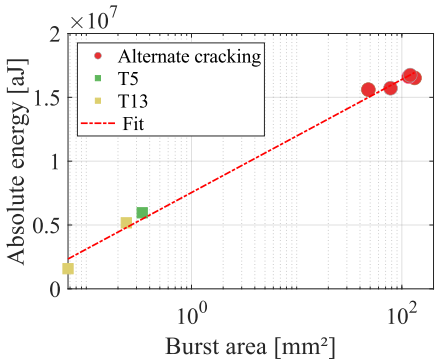


Figure 13: The AE absolute energy [aJ] as a function of the burst area (log-scale) for dynamic propagating cracks. Results are extended with data from alternate cracking experiments investigated in (Heinzmann et al., 2023).

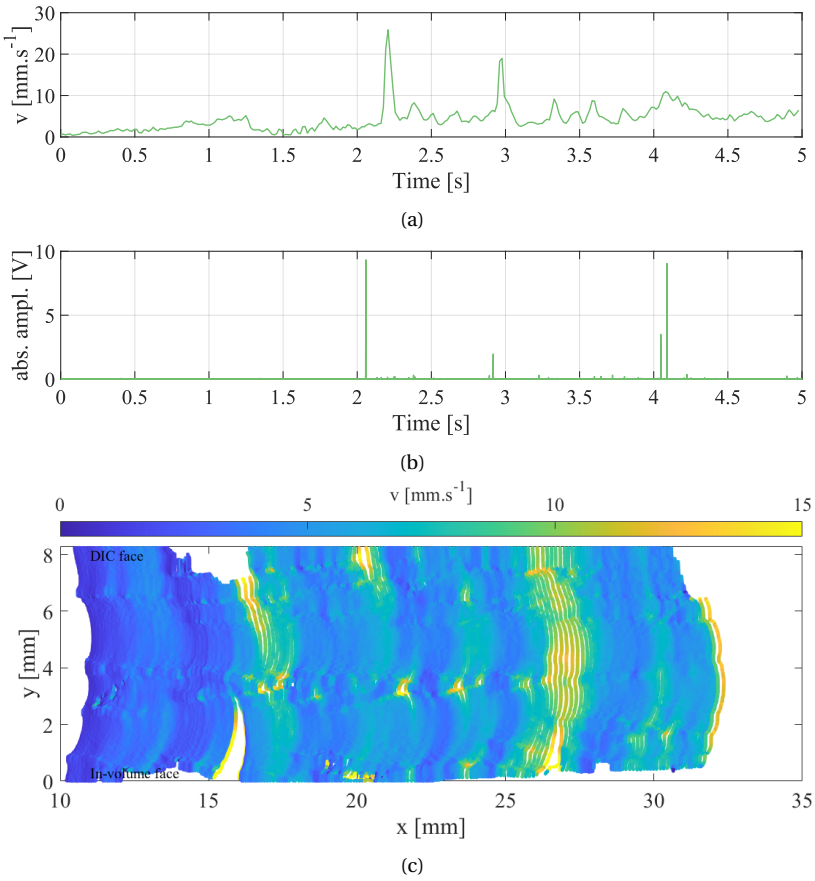


Figure 14: For experiment T13, (a) and (b) present, as a function of the recording time [s], DIC determined crack tip speed [mm.s$^{-1}$] and the absolute voltage signal of the AE streaming, respectively, while crack front velocities [mm.s$^{-1}$] along the sample thickness are shown in (c). Notice, white areas at the borders of the velocity map stem from the algorithm not being able to properly detect the edge of the crack front within the volume.

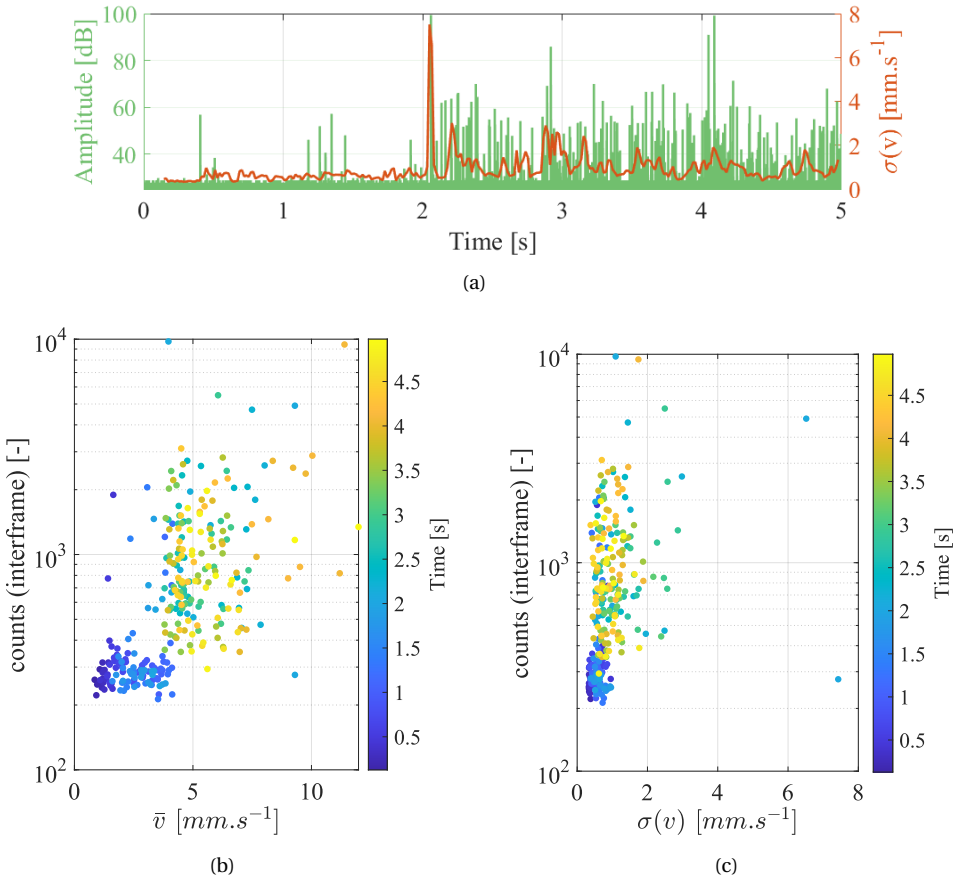


Figure 15: (a) AE streaming [dB] and the standard deviation ($\sigma$) of the velocity map [mm.s$^{-1}$] as a function of the recording time [s] for experiment T13. (b) and (c) present the interframe (16 ms) threshold (26 dB) crossings (counts) as a function of the mean ($\bar{v}$) and standard deviation ($\sigma(v)$) of the crack front velocity [mm.s$^{-1}$].

### *4.2.2. Lower amplitude (LA) signals*

After discussing the origin of apparent crack tip speed variations, HA signals evident relation to the localized dynamic instabilities, as well as clear connection between crack front velocity heterogeneity and the density/amplitude of AE signals, we will focus on the remaining lower amplitude (LA) signals. First of all, it is worthwhile mentioning that conclusions might differ with respect to the AE sensor used for performing the analysis. Even when the theoretical application of the AE method seems rather trivial, waves propagating at different velocities, while being reflected, dispersed and refracted, increases the difficulty of adequate interpretation of the recorded AE activity. Particularly in the

case of LA signals, the impact of each individual sensor, directionality of elastic waves due to crack front complexities or the attenuation of signals from different wave traveling distances result in the variation of waveform characteristics of the same AE signal for different sensors. This has similarly been pointed out by (Maillet et al., 2015) for the classification of damage modes in composite materials. To underline this, a LA example signal is presented in the Appendix C (Figure C.26) with their computed AE parameters (Table C.6) for all four sensors. With extensive literature existing on the investigation and classification of AE activity, the objective here is not to provide an exhaustive analysis of LA signals but underline, complementary to the previous part, intrinsic difficulties in properly associating AE responses to source mechanisms and their fingerprint on the fracture surface. Contrary to HA signals, where a straightforward link between apparent crack velocity variations, AE responses and fracture surface features can be established, LA signals are more numerous (somehow similarly spread along the entire recording), while potentially being associated to various and subtle fracture surface features. This section proposes to use the developed experiment and analysis tools to discuss this complex relationship.

Firstly, the fracture surface of the reference and complex cracking case will be compared by taking their AE activity into consideration. For this, a microscopic image of the post-mortem fracture surface of the two fracture cases are presented in Figure 16. On the one hand, with almost no AE activity (see Figure 8(a)), purely mode I cracking experiments in PMMA produce a surface with symmetric, wave like ligaments (see also (Hattali et al., 2012; Vasudevan, 2018)). These waves are found almost parallel to the crack propagation direction with a tendency to the boundaries, while showing topographical variations of approx. $\pm 70\ \mu$m. In addition, tiny regularly spaced waves (every $\sim$50-100 $\mu$m), perpendicular to the crack propagation, are observed. Theses waves may potentially be associated to small crack advances. On the other hand, deep and unstructured scratches on a rather flat fracture surface are observed during complex cracking cases, where strong AE activity is detected (see Figure 8(b) and (c)). At this stage, it seems reasonable to say that the change in AE activity is mainly due to the discrepancy observed at macro-scale, i.e. scratching marks.

For the classification of AE signals and their characteristics, plenty of analytical methods are proposed in literature (e.g. waveform cross-correlation (Deschanel et al., 2017), parametric clustering (Guo et al., 2017, 2022), wavelet analysis (Sung et al., 2000), b-value analysis (Sagar et al., 2012), moment tensor inversion (Grosse and Ohtsu, 2008)). For this study, the more specific method of multiplet identification through waveform cross-correlation (Deschanel et al., 2017) will be pursued. As the foundation of AE analysis, the

method relies on the assumption that similar waveforms are most likely related to the same source mechanism. The identification of multiplets directly compares signal characteristics by cross-correlating normalized waveforms to define highly correlated groups of signals, i.e. multiplets (nearly identical waveforms as signature of a unique source (Deschanel et al., 2017)). In the following, LA signals will be investigated by waveform cross-correlation with the aim of identifying AE signals, as in the case of HA signals, being linked to particular fracture surface markings. To present multiplets in the AE descriptor Principal Component (PC) space, signals were firstly normalized in this case. Indeed since multiplets are based on normalized waveforms, while e.g. amplitudes and energies may vary from one signal to another within a particular multiplet, direct comparison between AE feature and multiplet classification would be meaningless without an identical normalization in both techniques.

The identification of multiplets was performed only over the impulsive part, i.e. the duration of a signal free of rebounding waves. Thus, only primary waves will lead to the multiplet classification of signals. In the present case, the impulsive part was defined to be 40 $\mu$s starting from a 5 $\mu$s pre-trig preceding the detected time of arrival (TOA) of each waveform. A correlation coefficient above 0.75 was defined for the collection of AE multiplets.

Figure 17(a) is showing the signals associated to two multiplets in the space of the first and second principle component axis of the normalized AE parameters, with the contributions to the two principle components shown in Figure 17(b) and Figure 17(c), respectively. In the present case, due to normalization, some meaningless features have been removed from the analysis: Time and Threshold (as in the previous analysis of HA signals in Section 4.2.1), as well as Energy, Signal Strength and R-frequency (see Appendix B for feature details). When looking at Figure 17(a), clear multiplet separation is mainly observed along the first principal axis. Hence, taking Figure 17(b) into consideration, differentiation between AE signals associated to the two multiplets is driven by rise time, count and duration. However, it is worth mentioning that a classification, similar to multiplet, could not be achieved using neither k-means nor DBSCAN unsupervised classification methods. Different explanation could be proposed for such observation: (1) Multiplets are obtained from the impulsive part (40 $\mu$s), while the AE descriptor are computed using the entire waveform. Hence, the coda of the waveform makes the standard AE descriptor classification less straightforward. (2) Figure 17(a) shows that the entire set of lower amplitude signals are closely packed within the AE descriptor principal component space. Thus, no clear separation can be observed in between multiplets indicating that all signals share common features.

Furthermore, by identifying rise time, counts and duration as influential

waveform descriptors, one can define the RA-value (i.e. rise rime over amplitude) and relate it to the average frequency (counts over duration). Figure 18 is presenting all AE hits and the multiplets in the space of these two variables. For granular materials, the separation of AE hits in the space of average frequency and RA-value has been correlated to tensile and shear fracture modes (Aggelis, 2011; Noorsuhada et al., 2017). However, with limited information on the source activity in the case of PMMA, Figure 18 allows solely for highlighting the presence of two categories of AE signals, where the two multiplets are only represented in one.

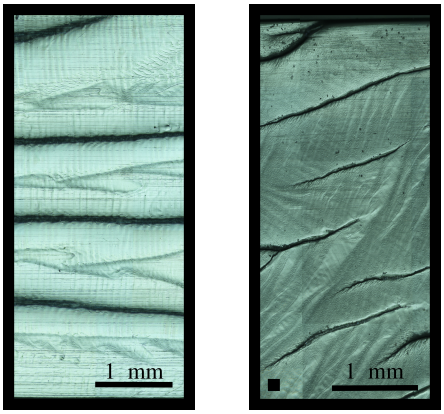


(a) (b)

Figure 16: Microscopic image of fracture surface for (a) reference and (b) complex (T5) cracking case. Crack propagation is from left to right.

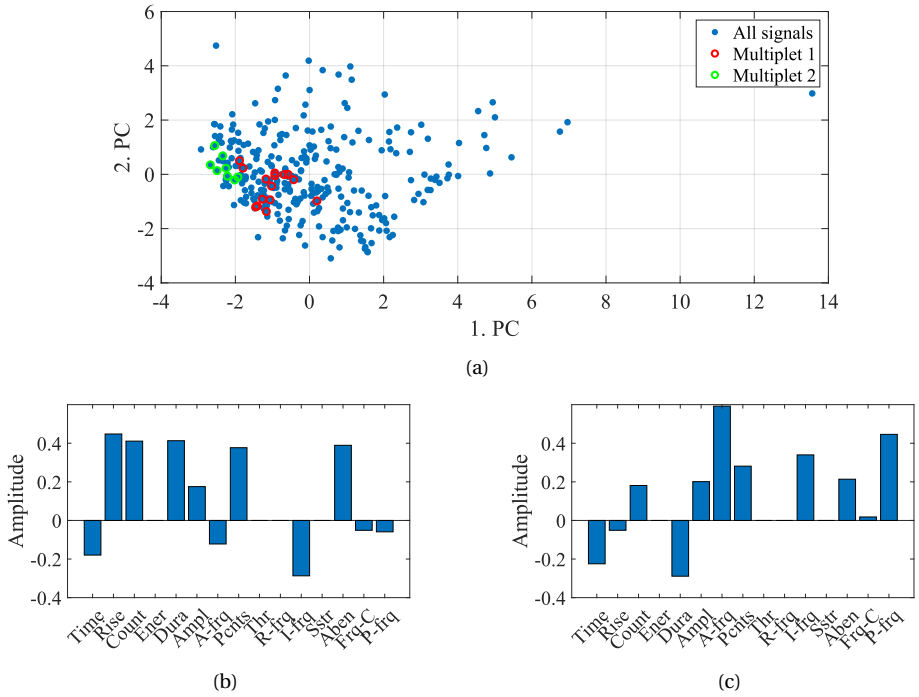


Figure 17: (a) Multiplet are presented in the space of first and second principle component axis of parameters computed from normalized AE signals, while (b) and (c) show the parametric contributions to the first and second principle component axis, respectively.

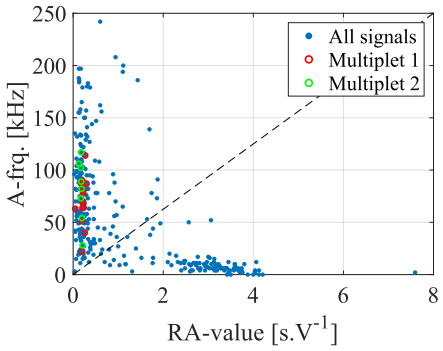


Figure 18: Average frequency [kHz] as a function of the RA-value (Rise Time over Amplitude) [s.V$^{-1}$].

*4.2.3. Multiplets vs fracture surface fingerprints*

The normalized waveforms of the two multiplets are presented next to the histogram of their correlation coefficients in Figure 19, while AE localization results are presented in Figure 20 to confirm the link between AE signals and crack tip activity. Indeed, waveforms associated to the two multiplets show to be highly similar over the duration of the defined impulsive part (40 $\mu$s). With an average correlation coefficient of 0.48 among all captured AE signals, average (and lowest) correlation coefficient of 0.88 (and 0.77) and 0.92 (and 0.83) were found among AE waveforms associated to Multiplet 1 and 2, respectively. Furthermore, information on the non-normalized waveforms presented in Figure 19 are presented in Table 5. The position of the multiplets on the fracture surface are shown in Figure 21. Notice that three signals (3-5) of Multiplet 1 appear within the same time frame and are thus linked to the same crack front. Hence, while 15 waveforms are collected in Multiplet 1, only 13 crack front lines are shown in Figure 21. Considering the high level of correlation between signals of a multiplet, one would expect to observe fingerprints of a similar source mechanisms during the fracture surface investigation. However, after inspecting the fracture surface in the vicinity of the expected source activity, no particular reoccurring surface mark is observed. For both multiplets, no repeating event can be unambiguously identified that is solely linked to their expected position of waveform formation. In an attempt to understand such observation, i.e. no clear macroscopic systematic fingerprint is observed at each crack front position associated to multiplet emissions, an extrapolation of Figure 12(b) is proposed. Indeed, following the observed linear relationship between AE absolute energies and the log of the growth fractured area in the case of dynamic instabilities (HA signals either macro or localized) and assuming similar mechanisms but at much smaller scale, an expected crack surface growth associated to multiplet signals can be estimated. With a difference in the dimension of millions between the AE absolute energy of LA signals (below 235 aJ, see Table 5) and HA signals (above $2\times10^6$ aJ), propagation areas below $\sim22.7\times10^3$ $\mu$m$^2$ will be associated to LA signals. In the case of a homogeneously propagating crack front, this would result in crack advances of approx. 2.8 $\mu$m over the sample thickness of 8 mm for the strongest LA signal. If expressed as a square with $\sim$151 $\mu$m sides, the sought for area is presented in Figure 16(b) in the left bottom corner as reference. This underlines the difficulty to unambiguously identify systematic similar fracture surface fingerprints for LA signals with the naked eye. However, while more advance image analysis tools may help, no obvious solution has been found in this work.

Nevertheless, Figure 15 has shown that link between AE and crack front

may be more connected to the actual kinematic of the crack front than on its post-mortem characteristics. To take advantage of the observations in Figure 15 for the correlation of AE activity with crack front velocity heterogeneity, Figure 22 is proposing an identification of potential locations of the AE signal origin on the fracture surface based on crack front velocity heterogeneity. For this, 22(a) shows, as reference, a fracture surface extraction of the crack propagation area during which the synchronized devices were active and 22(b) the velocity heterogeneity of the crack front for each frame of the inclined camera recording. The figure is supplemented with the AE hits positioned for HA signals at both, (1) the right time (i.e. within the crack front associated to this particular time) and (2) the velocity peak along the crack front and for LA signals just at (1) the right time (i.e. within the crack front associated to this particular time). Notice, while positioning HA signals onto the peak velocity along the crack front results in perfect identification of the source activity within the volume, one can not assume the same for LA signals, since the multiplet signal does not necessarily present the highest recorded AE signals associated to this frame.

Nevertheless, let us first focus only on the relation between the fracture surface and the crack front kinematics. Interestingly, no particular difference in terms of crack surface features can be identified with respect to the two phases of homogeneous (10-15 mm) and heterogeneous (15-32 mm) crack front propagation. However, velocity heterogeneity's – although different in scale – can be seen in both phases in the vicinity of the artifacts (white marks) on the fracture surface. Especially notable are the two local crack front jumps between two consecutive frames at approx. 15.5 mm and 27 mm that are associated to the first and second local dynamic instability, respectively. Extending the discussion by the AE waveforms, the two dynamic instabilities – being already well understood and localized during the previous discussion – are well identified (asterisk markers colored in magenta in Figure 22(b)) at the spatial position of the dynamic instability along the thickness of the sample. Noteworthy, the location of the dynamic instabilities has only been identified on the DIC face up to this point. Its correct fracture surface location was detected through pre-existing knowledge on fracture surface patterns associated to dynamic instabilities. However, by taking the above into consideration, before made assumptions have been evidenced.

With respect to AE signals being related to the multiplets, one can observe that all signals appear during the more 'responsive' section of the streaming (Figure 15) after the first dynamic instability. While the crucial information provided by the through thickness crack front growth rate heterogeneity seems to correlate the signals to local perturbations (scratches/artifacts) observed on the surface, it did not provide an unambiguous explanation for the natural

multiplet classification.

This section, while presenting a side discussion, is a perfect example of potential miss interpretation when dealing with partial AE data. Indeed, it is shown that a large amount of highly similar signals – coming from the crack tip – can not be systematically attributed, at least from post-mortem fracture surface features, to a particular mechanism or behavior. While discriminating fracture phenomena on signal levels has been found to be straightforward, classifying within signals of similar amplitudes have been found potentially misleading.

Table 5: Information on non-normalized waveforms associated to the multiplets.

| Multiplet | Peak amplitude range | Absolute Energy range (mean) |
|---|---|---|
| 1 | 8.9 mV (39 dB) to 50 mV (54 dB) | 7 aJ to 235 aJ (63 aJ) |
| 2 | 7.9 mV (38 dB) to 25 mV (48 dB) | 4 aJ to 50 aJ (28 aJ) |

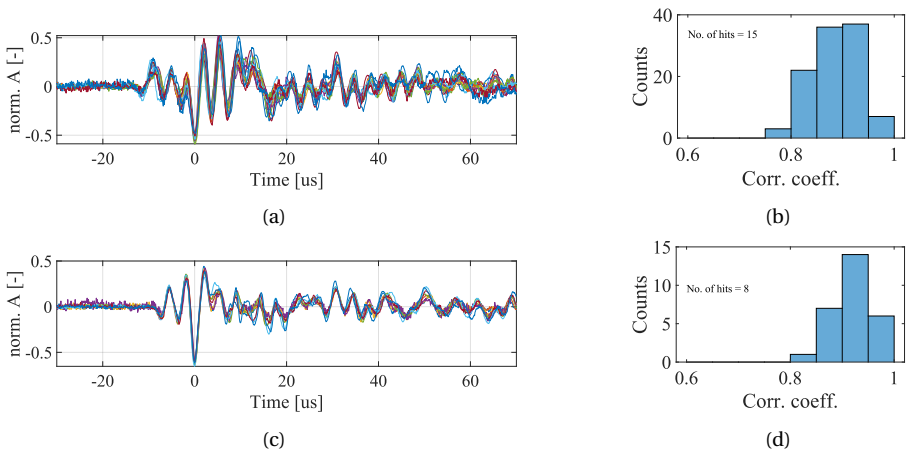


Figure 19: Normalized waveforms associated to (a) multiplet 1 and (c) multiplet 2, with their corresponding histogram of correlation coefficients ((b) and (d)).

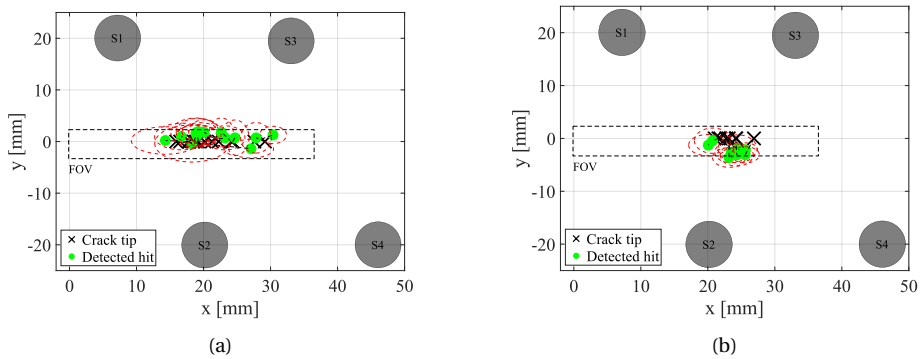


Figure 20: AE localization of (a) Multiplet 1 and (b) Multiplets 2.

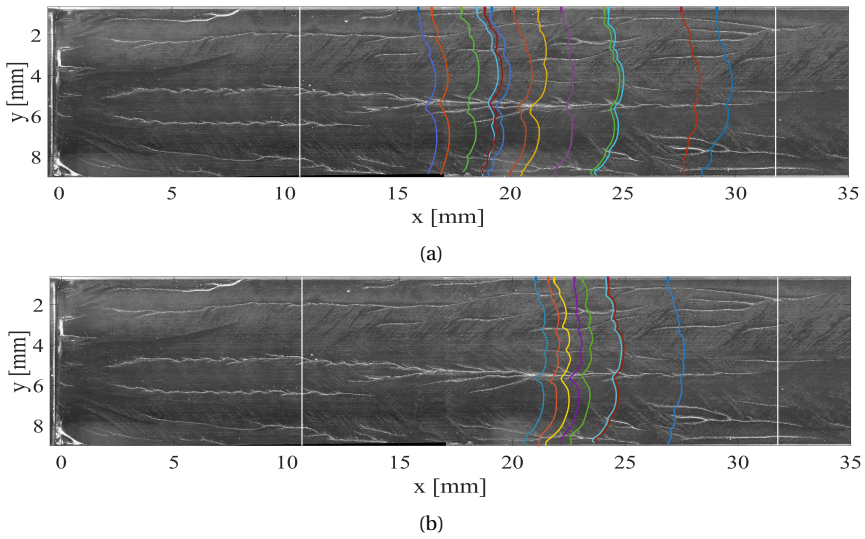


Figure 21: Crack front complexities related to waveforms associated with (a) Multiplet 1 and (b) Multiplet 2.

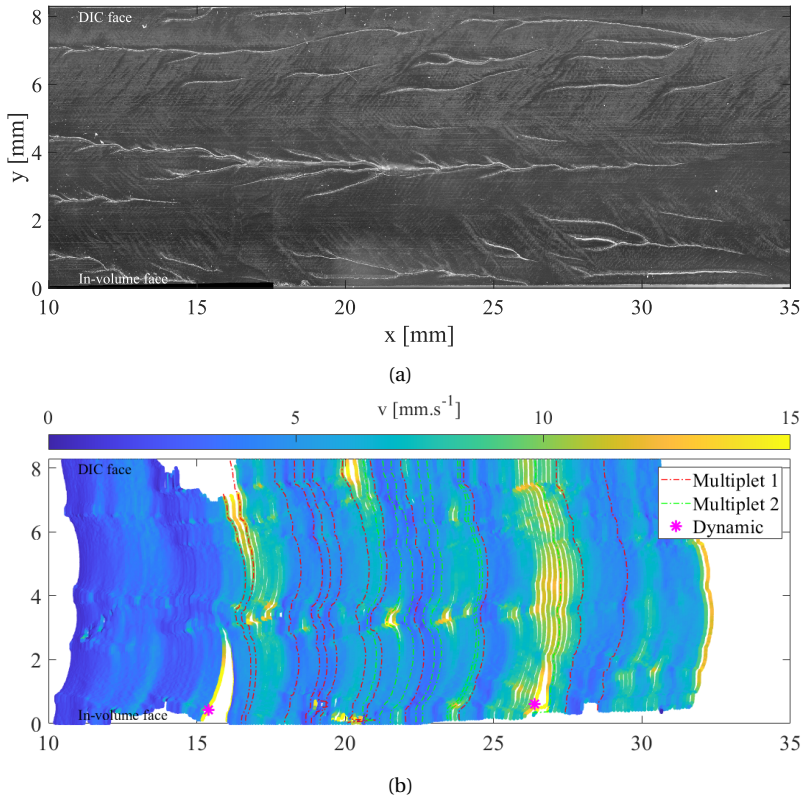


Figure 22: (a) Fracture surface crop over which the crack propagated during the experimental time and (b) corresponding crack front velocities [mm.s$^{-1}$] presented on the extracted crack fronts from the inclined images.

## 5. Conclusion and perspectives

A model lab experiment under mode I dominating opening mode – with slight front/back opening asymmetry leading to complex cracking behavior and high AE activity – has been designed and studied through a multiple point view perspective. With the aim of linking source mechanisms of AE signals to post-mortem fracture surface characteristics, the combination of devices allowed for a holistic investigation of the fracturing process. DIC, in-volume recordings and the combination of multiple AE sensor was used for crack tip detection, identification of crack front complexities/kinematics and AE source localization, respectively. The analysis relies on both, automatic crack tip detection using DIC and Williams series expansion, as well as AE source localization.

The present work provides (1) a methodological/numerical and (2) physical contribution that are summarized in the following:

1. On the methodological side, it has been shown that:

    - The ill-posed problem of AE localization, without a priori knowledge on the wave speed, using multiple AE sensor is highly sensitive to the initial guess when solving it with classical Newton-Raphson algorithms. This issue can be partly overcome by designing an optimization procedure for the initial guess. It has been done finding for each crack tip position the best initial guess parameters for convergence using a simple numerical twin. Eventually, for the sensor position considered in this work (not optimized), a localization uncertainty lower than 2 mm can be achieved for most of the crack propagation.
    - An image analysis procedure has been proposed to capture the position and the kinematics of complex crack front using in-volume recording in the case of a transparent material. It allows for capturing local variation of the crack front kinematics, which has been found highly valuable for connecting macroscopic AE activity and crack front behavior.
    - The combination of in-volume observations and apparent crack tip position from LEFM theory and DIC, it has been shown that the apparent crack tip position is closely related to the surface crack front position and does not reflect crack front complexity by a through thickness homogenization process. This point remained unclear in the literature associated to crack tip detection using William's series expansion and DIC.

2. On the physical interpretation side, the following points have been observed:

    - A systematic connection between AE activity and crack front position has been demonstrated using both apparent crack tip detection, through DIC/Williams' series expansion, and AE localization.
    - Combining AE streaming and in-volume crack front kinematics data, a strong correlation between amount and intensity of acoustic emission and heterogeneity of the crack front kinematics has been observed. Indeed, while homogeneous crack front velocity does not

produce signals, at least high enough to leave noise floor, once the crack front kinematics become heterogeneous, strong AE activity occurred. It explains the difference in term of AE activity observed between pure mode I and perturbed mode I experiments in PMMA. This observation is highly valuable since it demonstrates that post-mortem analysis could be misleading in term of AE source mechanism analysis, since it does not necessarily reflects the transient kinematics of the front.

- Different families of AE signals have been observed: High amplitude (HA), a dominant class of lower amplitude (LA) signals and among them two multiplets, i.e. set of signals having highly correlated impulsive waveform parts.
- A connection between dynamic instabilities of intermittent stick-slip phenomenon produced macroscopically in PMMA when crack growth rates reach the forbidden velocity domain (see (Heinzmann et al., 2023)) and of the front/back asymmetric experiments during dominant mode I loading was presented. Both produce significantly higher AE signals compared to any other crack front relared AE activity, while their particular fracture surface pattern evidenced local velocities around 30-200 $m.s^{-1}$ (see (Heinzmann et al., 2023)).
- A linear relationship between AE absolute energy of HA signals and the log of the fracture growth area has been found considering both: the present localized dynamic instabilities and macroscopic stick-slip phenomenon investigated in the previous work (see (Heinzmann et al., 2023)). An attempt of extrapolation, from this relationship to LA signals, has been done leading to potential fracture growth area of about $150 \times 150$ $\mu$m. It may evidence that LA emission are rather induced by localized small crack growth than macroscopic crack advance.
- Two important multiplets have been observed composed of 15 and 8 successive AE signals with highly correlated impulsive waveform parts. While their impulsive parts clearly characterize them, it has been found difficult to find a similar classification using standard procedures such as k-means or DBSCAN clustering algorithms of the waveforms in the dominand PC space of the AE descriptors. Indeed most of the LA signals share close characteristics, and considering the entire wave form instead of only the impulsive part makes classification difficult.

- No clear relationship between post-mortem fracture surface features, transient crack front kinematics and multiplets, or systematical identification of source mechanisms has been found, which reflects the complexity of classifying (especially in a blind NDT approach) AE signals sharing similar AE amplitudes. A proposition has been done, linking AE to localized crack front accelerations in line with the HA signal analysis and AE/velocity heterogeneity observations done macroscopically. However, conclusions remain vague.

This paper has demonstrated that combining different investigation tools – surface and in-volume imagine, AE and post-mortem analysis – AE sources and the crack front can be undoubtedly connected for AE signals with extreme characteristics such as dynamic instabilities. However, classification of LA signals, dominant during quasi-static crack propagation, remains highly difficult to connect unambiguously to a particular source mechanism even for highly correlated wavesforms successively reappearing along 15 mm of crack propagation. We do believe that such lab experiment may help the design of NDT algorithm discriminating in-real time different AE sources. Nevertheless, to completely shed light on all blind-spots in the process of AE source identification, one would need to account for the visualization of elastic waves traveling from their source to the transducer. Here, the presented experimental campaign would need to be extended by an ultra-high speed imaging device with potential high spatial resolution (Vinel et al., 2021). However, with expected strain levels induced by the energy released during small crack propagation, this remains a significant experimental challenge.

## Acknowledgement

The authors gratefully acknowledge the support of the Agence Nationale de la Recherche (ANR) through grant ANR-19-CE42-0012.

## Declarations

*Conflict of interest:*

No conflict of interest is declared by the authors.

## Appendix A. Fracture parameters by DIC

The foundation for retrieving the sought-after fracture mechanics variables is found in DIC by providing fullfield displacement measurements from sequential images. By following the principle of conservation of brightness between a reference ($f$) and a deformed image ($g$), i.e. the equation of optical flow, DIC presents an ill-posed non-linear inverse problem:

$$f(\underline{X}) = g(\underline{X} + \underline{u}(\underline{X})) \tag{A.1}$$

with $\underline{u}(\underline{X})$ being the sought displacement field. To bypass this ill-posed problem, the pixel displacement has to be parameterized using shape functions. Here, FE discretization has been used (Besnard et al., 2006). Eventually, the problem can be linearized and solved iteratively in a least-squares sense. A median regularization is used to mitigate detrimental impact of noise and smaller elements. By post-treating the displacement field, variables relevant for fracture mechanics analysis (e.g. SIFs and crack tip positions) were derived through Williams' series expansion. Traditionally, in the case of a semi infinite linear elastic isotropic media, stress and displacement fields around the crack tip depend on SIF, the distance to the crack tip ($r$) and the angle ($\theta$) in a polar reference system attached to the crack tip (Williams, 1957). Thus, by knowing the displacement field through DIC and projecting it onto the analytical solution, different fracture mechanics parameters can be derived through a non-linear inverse problem (Roux and Hild, 2006; Réthoré, 2015; Roux-Langlois et al., 2015). The displacement field around the crack tip is written as following:

$$u(r,\theta) = \sum_{i=I,II} \sum_{n=-\infty}^{\infty} A_i^n \, r^{n/2} g_i^n(\theta) \tag{A.2}$$

with the distance to the crack tip $r$, the angle $\theta$ in a polar reference system attached to the crack tip, Williams' coefficients $A$ and base function $g$. The base function $g_i^n(\theta)$ has the following form:

$$g_I^n(\theta) = \frac{1}{2\mu} \begin{bmatrix} (\kappa + n/2 + (-1)^n) cos[(n/2)\theta] - (n/2) cos[(n/2-2)\theta] \\ (\kappa - n/2 - (-1)^n) sin[(n/2)\theta] + (n/2) sin[(n/2-2)\theta] \end{bmatrix}_{(e_t, e_n)} \tag{A.3}$$

$$g_{II}^n(\theta) = \frac{1}{2\mu} \begin{bmatrix} -(\kappa + n/2 - (-1)^n) sin[(n/2)\theta] + (n/2) sin[(n/2-2)\theta] \\ (\kappa - n/2 - (-1)^n) cos[(n/2)\theta] + (n/2) cos[(n/2-2)\theta] \end{bmatrix}_{(e_t, e_n)} \tag{A.4}$$

with $\mu$ and $\kappa$ being the shear modulus and the Kolossov's constant, respectively. Kolossov's constant under plane stress is $\kappa = (3-\nu)/(1+\nu)$ with $\nu$ being the Poisson's ratio.

Equation A.2 states, that displacements can be computed for an infinite sum of modes. However, limiting the solution to $n_{min}$ = -3 and $n_{max}$ = 7 is sufficient to retain the relevant crack features. For quasi-brittle medium, good agreement of the mechanical fields can be established outside the process zone of the crack for the following Williams' series coefficient ($A_i^n$) solutions:

n = 0, in-plane rigid body translations

n = 1, asymptotic terms $K_I$ and $K_{II}$

n = 2, T-stress and in-plane body rotations

Notice that the projection zone (Figure 6) is defined by $R_{min}$ and $R_{max}$. On the one hand, the asymptotic behaviour near the crack tip of the fields computed by the super-singular terms ($n$ <0) do not provide any physical meaning and are therefore classically neglected. However, when the crack tip position is sought, these super-singular functions appear in the required basis ($n$=-1 being, up to a scaling factor, the derivative of $n$=1 with respect to the assumed crack tip position). To not induce biases due to truncation, terms for $n$ down to -3 are considered. Hence, data at a distance to the crack tip smaller than $R_{min}$ are discarded to maintain reasonable conditioning of the least-squares problem. On the other hand, $R_{max}$ – defining the projection zone size externally – has to be small enough to avoid influences of the free boundary, but large enough to still include a sufficient amount of mesh points in the domain. The right size of projection zone, i.e. defining $R_{min}$ and $R_{max}$ (see Table 3), has been identified through a parametric study. Furthermore, by using a predefined crack path, the super-singular term n = -1 is used to estimate the position to the equivalent elastic crack tip along this path (Réthoré et al., 2011).

## Appendix B. Principle component analysis

In AE analysis, 16 AE waveform parameters are computed by the AE system. They are used as waveform descriptors to define the characteristics of each AE hit. The descriptors are defined as following:

- Amplitude - highest voltage in the AE waveform, expressed on the dB AE amplitude scale.
- Energy - time integral of the absolute signal voltage. The reported magnitude, depends on the value selected for Energy Reference Gain. Proportional to Signal Strength.

- Counts - number of times the signal crosses the detection threshold.
- Duration - time from first to last threshold crossing (µs).
- RMS - root mean square voltage during a period of time based on a software programmable time constant, referred to the input to the signal processing board.
- ASL - RMS, converted to the dB AE scale (0dB AE = 1µV at the sensor, before any amplification).
- Threshold - detection threshold, on the dB AE scale.
- Rise Time - time from first threshold crossing to highest voltage point on the waveform (µs).
- Counts to Peak - number of threshold crossings from first to highest voltage point on the waveform.
- Average Frequency - Counts divided by Duration, divided by 1000 (thus, kHz). Note that this is not a spectral domain calculation, but a calculation from time domain features.
- Reverberation Frequency - (Counts - Counts to Peak) divided by (Duration - Risetime). .
- Initiation Frequency - Counts to Peak divided by Risetime.
- Signal Strength - time integral of the absolute signal voltage, expressed in pVs (picovolt-seconds) referenced to the sensor, before any amplification. Proportional to Energy.
- Absolute Energy - time integral of the square of the signal voltage at the sensor before any amplification, divided by a $10k\Omega$ impedance and expressed in aJ (attojoules).
- Frequency centroid - the center of mass of the power spectrum graph.
- Peak frequency - the point where the power spectrum is greatest.

These descriptors are being used to identify similarities among different AE responses and thereby help linking them to physical, chemical and/or mechanical source mechanisms. In literature and industry, different methods are being used to distinguish among sets of AE responses. Here, the Mistras group software Noesis has been taken as reference and replicated in Matlab. The following methodology has then been pursued, presented on example data:

1. *Correlation matrix of waveform descriptors*
Here, a Pearson (Freedman, David et al., 2007) pairwise linear correlation between each pair of columns, i.e. waveform descriptors, has been performed as followed:

$$\rho(a,b) = \frac{\sum_{i=1}^{n}(X_{a,i} - \overline{X_a})(X_{b,i} - \overline{X_b})}{[\sum_{i=1}^{n}(X_{a,i} - \overline{X_a})^2 \sum_{j=1}^{n}(X_{b,j} - \overline{X_b})^2]^{1/2}}, \tag{B.1}$$

with

$$\overline{X_a} = \frac{\sum_{i=1}^{n} X_{a,i}}{n} \tag{B.2}$$

and

$$\overline{X_b} = \frac{\sum_{j=1}^{n} X_{b,j}}{n}, \tag{B.3}$$

where $X_a$ and $X_b$ are columns in the parametric matrix, while n is the length of the column.

2. *Dendrogram plot of correlation matrix*
The degree of correlation between the features of the data set has then been displayed in the form of a dendrogram. With the most correlated features joined together at the top, the degree of correlation decreases towards the bottom of the graph. This has been done to narrow down the amount of descriptors to be used for clustering and hence neglect descriptors with similar tendencies. The dendrogram plot is presented in Figure B.23. Descriptors that have high coefficients of correlation (again, 1.0 being the maximum) are linked at their value of correlation and can thereby be identified.

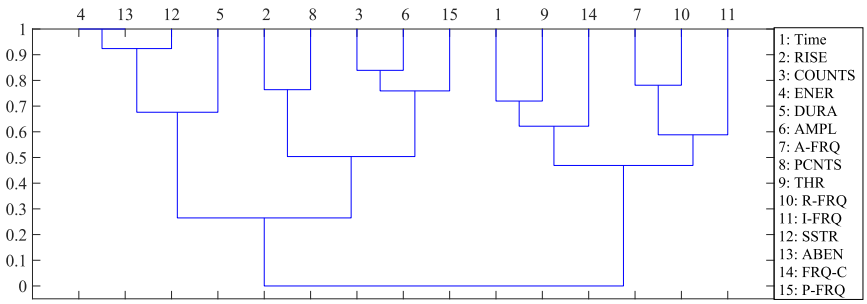


Figure B.23: Correlation matrix of waveform descriptors presented as dendrogram.

In this example, very strong correlation is found between Energy and Absolute Energy, which would allow the user to neglect one of them to reduce complexity without loosing information. Remaining parameters are then used for the continuation of the analysis.

3. *Principle components analysis*
The principle component analysis (Karamizadeh et al., 2013) has been applied to increase understanding of the AE observation. In a first step, the most relevant principle components have to be identified.

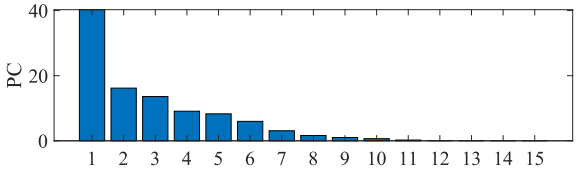


Figure B.24: Evaluation of most influential principle component axes.

Based on the example case of a typical PCA of waveform descriptors presented in Figure B.24, the first and second principle components contribute the most to the differentiation of the waveforms. Thus, investigated data would best be visualized in the space of the two axis. Their contribution by each AE parameter is presented in Figure B.25.

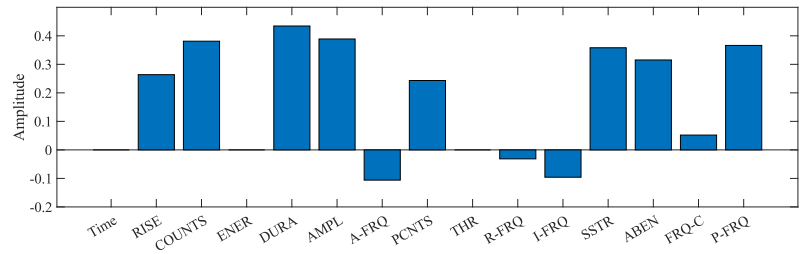


(a)

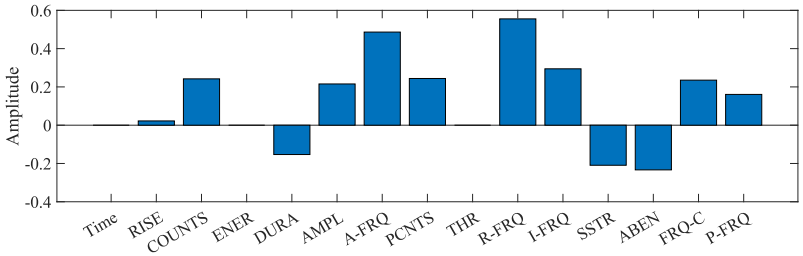


(b)

Figure B.25: Feature contributions to the (a) first and (b) second principle component axis.

## Appendix C. Sensor comparison

This appendix presents a particular AE signal – extracted from a multiplet – received at all four sensors. Figure C.26 shows the same signal detected at all four sensors for (a) 300 $\mu$s and (b) 40 $\mu$s (impulsive) of the entire signal duration. The threshold is indicated by the red dashed lines. AE parameters of the signal computed for all four sensors are presented in Figure C.6. Figure C.26(b) corresponds to a signal being presented in the core of paper in Figure 19 associated to Multiplet 1.

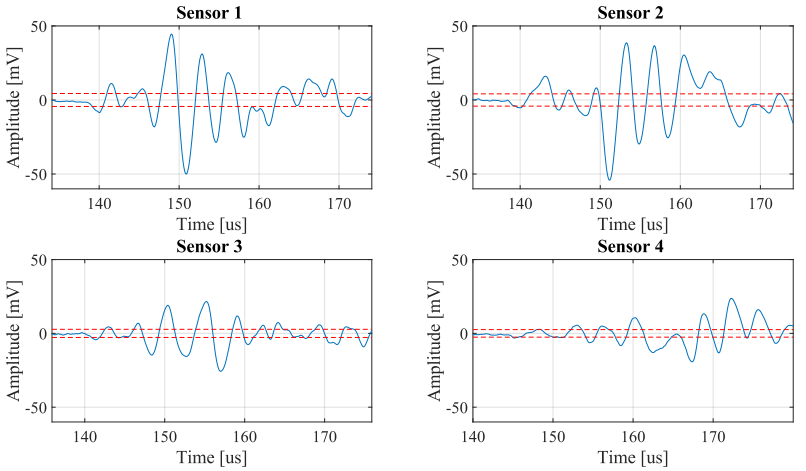


(a)

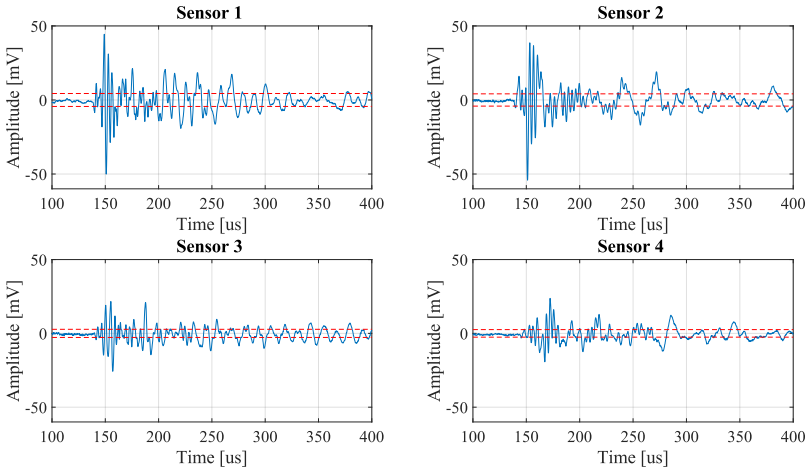


(b)

Figure C.26: Same signal detected at all four sensors for (a) 300 $\mu$s and (b) 40 $\mu$s (coda) of the signal. The threshold is indicated by the red dashed lines.

Table C.6: AE parameters computed for the signal in Figure C.26 in chronological order of the sensor number.

| Time | RISE | COUN | ENER | DURA | AMP | A-FRQ | PCNTS | THR | R-FRQ | I-FRQ | SIG STR | ABS-ENER | FRQ-C | P-FRQ |
|---|---|---|---|---|---|---|---|---|---|---|---|---|---|---|
| 2.4769143 | 12 | 27 | 3 | 975 | 53 | 28 | 3 | 31 | 25 | 250 | 2606.29 | 19.72 | 1904 | 106 |
| 2.4769145 | 12 | 31 | 2 | 975 | 52 | 32 | 3 | 31 | 29 | 250 | 2169.2 | 17.21 | 1449 | 41 |
| 2.4769161 | 17 | 32 | 2 | 973 | 47 | 33 | 4 | 31 | 29 | 235 | 1773.92 | 8.07 | 1276 | 93 |
| 2.4769203 | 28 | 27 | 2 | 969 | 48 | 28 | 6 | 31 | 22 | 214 | 1795.97 | 7.3 | 1667 | 1 |

As precised in the core of the text, we can observe that the same source event can produce a significantly different signal on each sensors. While all the analysis in the paper has been done on Sensor 2, it shows that performing the analysis on different sensor may lead to slightly different results in term of classification and multiplet detection. In the present case, Sensor 1 and Sensor 2 are systematically behind the crack front, while Sensor 3 and Sensor 4 are in front. We observe that the main difference, in terms of impulsive response (see Figure C.26(b)), is observed between signals in front or behind the source, which potentially evidences a clear directionality of the wave propagating. It underlines the complexity of analysis and classifying, in a bulk, crack propagating, branching, turning with respect to the sensors.

## References


Abel, J., Smith, J., 1987. The spherical interpolation method for closed-form passive source localization using range difference measurements, in: ICASSP '87. IEEE International Conference on Acoustics, Speech, and Signal Processing, Institute of Electrical and Electronics Engineers, Dallas, TX, USA. pp. 471–474. URL: http://ieeexplore.ieee.org/document/1169674/, doi:10.1109/ICASSP.1987.1169674.

Aggelis, D.G., 2011. Classification of cracking mode in concrete by acoustic emission parameters. Mechanics Research Communications 38, 153–157. URL: https://linkinghub.elsevier.com/retrieve/pii/S0093641311000620, doi:10.1016/j.mechrescom.2011.03.007.

Almeida, R.S., Magalhães, M.D., Karim, M.N., Tushtev, K., Rezwan, K., 2023. Identifying damage mechanisms of composites by acoustic emission and supervised machine learning. Materials & Design 227, 111745. URL: https://linkinghub.elsevier.com/retrieve/pii/S0264127523001600, doi:10.1016/j.matdes.2023.111745.

Arnau, A., Soares, D., 2008. Fundamentals of Piezoelectricity, in: Vives, A.A. (Ed.), Piezoelectric Transducers and Applications. Springer Berlin Heidelberg, Berlin, Heidelberg, pp. 1–38. URL: http://link.springer.com/10.1007/978-3-540-77508-9_1, doi:10.1007/978-3-540-77508-9_1.

Arumugam, V., Barath Kumar, S., Joseph Stanley, A., 2011. Effect of fuzzy C means technique in failure mode discrimination of glass/epoxy laminates using acoustic emission monitoring. Russ J Nondestruct Test 47, 858–864.

URL: http://link.springer.com/10.1134/S1061830911120035, doi:10.1134/S1061830911120035.

Besnard, G., Hild, F., Roux, S., 2006. "Finite-Element" Displacement Fields Analysis from Digital Images: Application to Portevin–Le Châtelier Bands. Exp Mech 46, 789–803. URL: http://link.springer.com/10.1007/s11340-006-9824-8, doi:10.1007/s11340-006-9824-8.

Bonamy, D., Ravi-Chandar, K., 2003. Interaction of Shear Waves and Propagating Cracks. Phys. Rev. Lett. 91, 235502. URL: https://link.aps.org/doi/10.1103/PhysRevLett.91.235502, doi:10.1103/PhysRevLett.91.235502.

Cao, Z., Wang, B.F., Wang, K.M., Lin, H.G., Yu, R.Q., 1998. Chemical acoustic emissions from gas evolution processes recorded by a piezoelectric transducer. Sensors and Actuators B: Chemical 50, 27–37. URL: https://linkinghub.elsevier.com/retrieve/pii/S092540059800152X, doi:10.1016/S0925-4005(98)00152-X.

Cheng, L., Xin, H., Groves, R.M., Veljkovic, M., 2021. Acoustic emission source location using Lamb wave propagation simulation and artificial neural network for I-shaped steel girder. Construction and Building Materials 273, 121706. URL: https://linkinghub.elsevier.com/retrieve/pii/S0950061820337107, doi:10.1016/j.conbuildmat.2020.121706.

Ciaburro, G., Iannace, G., 2022. Machine-Learning-Based Methods for Acoustic Emission Testing: A Review. Applied Sciences 12, 10476. URL: https://www.mdpi.com/2076-3417/12/20/10476, doi:10.3390/app122010476.

Ciampa, F., Meo, M., 2010. A new algorithm for acoustic emission localization and flexural group velocity determination in anisotropic structures. Composites Part A: Applied Science and Manufacturing 41, 1777–1786. URL: https://linkinghub.elsevier.com/retrieve/pii/S1359835X10002332, doi:10.1016/j.compositesa.2010.08.013.

Crandall, D., Moore, J., Gill, M., Stadelman, M., 2017. CT scanning and flow measurements of shale fractures after multiple shearing events. International Journal of Rock Mechanics and Mining Sciences 100, 177–187. URL: https://linkinghub.elsevier.com/retrieve/pii/S136516091630449X, doi:10.1016/j.ijrmms.2017.10.016.

Dehghan Niri, E., Salamone, S., 2012. A probabilistic framework for acoustic emission source localization in plate-like structures. Smart Mater. Struct. 21, 035009. URL: https://iopscience.iop.org/article/10.1088/0964-1726/21/3/035009, doi:10.1088/0964-1726/21/3/035009.

Deschanel, S., Ben Rhouma, W., Weiss, J., 2017. Acoustic emission multiplets as early warnings of fatigue failure in metallic materials. Sci Rep 7, 13680. URL: http://www.nature.com/articles/s41598-017-13226-1, doi:10.1038/s41598-017-13226-1.

Dong, L., Zou, W., Sun, D., Tong, X., Li, X., Shu, W., 2019. Some Developments and New Insights for Microseismic/Acoustic Emission Source Localization. Shock and Vibration 2019, 1–15. URL: https://www.hindawi.com/journals/sv/2019/9732606/, doi:10.1155/2019/9732606.

Freedman, David, Pisani, Robert, Purves, Roger, Adhikari, Ani, 2007. Statistics. WW Norton & Company New York .

Gonzalez, R.C., Eddins, S.L., Woods, R.E., 2004. Digital image publishing using MATLAB. Prentice Hall.

Grosse, C., Ohtsu, M. (Eds.), 2008. Acoustic Emission Testing. Springer Berlin Heidelberg, Berlin, Heidelberg. URL: http://link.springer.com/10.1007/978-3-540-69972-9, doi:10.1007/978-3-540-69972-9.

Guo, M., Alam, S.Y., Bendimerad, A.Z., Grondin, F., Rozière, E., Loukili, A., 2017. Fracture process zone characteristics and identification of the microfracture phases in recycled concrete. Engineering Fracture Mechanics 181, 101–115. URL: https://linkinghub.elsevier.com/retrieve/pii/S001379441730406X, doi:10.1016/j.engfracmech.2017.07.004.

Guo, Y., Shang, D., Zuo, L., Qu, L., Hou, G., Cai, D., Jin, T., Yin, X., 2022. Identification of fatigue damage modes for carbon fiber/epoxy composites using acoustic emission monitoring under fully reversed loading. Polymer Composites 43, 3371–3385. URL: https://onlinelibrary.wiley.com/doi/10.1002/pc.26622, doi:10.1002/pc.26622.

Hamam, R., Hild, F., Roux, S., 2007. Stress Intensity Factor Gauging by Digital Image Correlation: Application in Cyclic Fatigue. Strain 43, 181–192. URL: https://onlinelibrary.wiley.com/doi/10.1111/j.1475-1305.2007.00345.x, doi:10.1111/j.1475-1305.2007.00345.x.

Hassan, F., Mahmood, A.K.B., Yahya, N., Saboor, A., Abbas, M.Z., Khan, Z., Rimsan, M., 2021. State-of-the-Art Review on the Acoustic Emission Source Localization Techniques. IEEE Access 9, 101246–101266. URL: https://ieeexplore.ieee.org/document/9481912/, doi:10.1109/ACCESS.2021.3096930.

Hattali, M., Barés, J., Ponson, L., Bonamy, D., 2012. Low Velocity Surface Fracture Patterns in Brittle Material: A Newly Evidenced Mechanical Instability. MSF 706-709, 920–924. URL: https://www.scientific.net/MSF.706-709.920, doi:10.4028/www.scientific.net/MSF.706-709.920.

Heinzmann, R., Seghir, R., Alam, S.Y., Réthoré, J., 2023. Experimental investigation of the alternate recurrence of quasi-static and dynamic crack propagation in PMMA. URL: https://hal.science/hal-03975862. working paper or preprint.

Henninger, C., Roux, S., Hild, F., 2010. Enriched kinematic fields of cracked structures. International Journal of Solids and Structures 47, 3305–3316. URL: https://linkinghub.elsevier.com/retrieve/pii/S002076831000291X, doi:10.1016/j.ijsolstr.2010.08.012.

Hensman, J., Mills, R., Pierce, S., Worden, K., Eaton, M., 2010. Locating acoustic emission sources in complex structures using Gaussian processes. Mechanical Systems and Signal Processing 24, 211–223. URL: https://linkinghub.elsevier.com/retrieve/pii/S0888327009001885, doi:10.1016/j.ymssp.2009.05.018.

Jayakumar, T., Mukhopadhyay, C., Venugopal, S., Mannan, S., Raj, B., 2005. A review of the application of acoustic emission techniques for monitoring forming and grinding processes. Journal of Materials Processing Technology 159, 48–61. URL: https://linkinghub.elsevier.com/retrieve/pii/S0924013604000615, doi:10.1016/j.jmatprotec.2004.01.034.

Karamizadeh, S., Abdullah, S.M., Manaf, A.A., Zamani, M., Hooman, A., 2013. An Overview of Principal Component Analysis. JSIP 04, 173–175. URL: http://www.scirp.org/journal/doi.aspx?DOI=10.4236/jsip.2013.43B031, doi:10.4236/jsip.2013.43B031.

Kong, Y., Bennett, C., Hyde, C., 2020. A review of non-destructive testing techniques for the in-situ investigation of fretting fatigue cracks. Materials & Design 196, 109093. URL: https://linkinghub.elsevier.com/retrieve/pii/S0264127520306286, doi:10.1016/j.matdes.2020.109093.

Li, L., Lomov, S.V., Yan, X., Carvelli, V., 2014. Cluster analysis of acoustic emission signals for 2D and 3D woven glass/epoxy composites. Composite Structures 116, 286–299. URL: https://linkinghub.elsevier.com/retrieve/pii/S0263822314002335, doi:10.1016/j.compstruct.2014.05.023.

Maillet, E., Baker, C., Morscher, G.N., Pujar, V.V., Lemanski, J.R., 2015. Feasibility and limitations of damage identification in composite materials using acoustic emission. Composites Part A: Applied Science and Manufacturing 75, 77–83. URL: https://linkinghub.elsevier.com/retrieve/pii/S1359835X15001499, doi:10.1016/j.compositesa.2015.05.003.

Noorsuhada, M.N., Abdul Hakeem, Z., Soffian Noor, M.S., Noor Syafeekha, M.S., Azmi, I., 2017. Correlation between average frequency and RA value (rise time/amplitude) for crack classification of reinforced concrete beam using acoustic emission technique, Langkawi, Malaysia. p. 050001. URL: https://pubs.aip.org/aip/acp/article/886503, doi:10.1063/1.5010497.

Ravi-Chandar, K., Balzano, M., 1988. On the mechanics and mechanisms of crack growth in polymeric materials. Engineering Fracture Mechanics 30, 713–727. URL: https://linkinghub.elsevier.com/retrieve/pii/0013794488901610, doi:10.1016/0013-7944(88)90161-0.

Romhány, G., Czigány, T., Karger-Kocsis, J., 2017. Failure Assessment and Evaluation of Damage Development and Crack Growth in Polymer Composites Via Localization of Acoustic Emission Events: A Review. Polymer Reviews 57, 397–439. URL: https://www.tandfonline.com/doi/full/10.1080/15583724.2017.1309663, doi:10.1080/15583724.2017.1309663.

Roux, S., Hild, F., 2006. Stress intensity factor measurements from digital image correlation: post-processing and integrated approaches. Int J Fract 140, 141–157. URL: http://link.springer.com/10.1007/s10704-006-6631-2, doi:10.1007/s10704-006-6631-2.

Roux, S., Réthoré, J., Hild, F., 2009. Digital image correlation and fracture: an advanced technique for estimating stress intensity factors of 2D and 3D cracks. J. Phys. D: Appl. Phys. 42, 214004. URL: https://iopscience.iop.org/article/10.1088/0022-3727/42/21/214004, doi:10.1088/0022-3727/42/21/214004.

Roux-Langlois, C., Gravouil, A., Baietto, M.C., Réthoré, J., Mathieu, F., Hild, F., Roux, S., 2015. DIC identification and X-FEM simulation of fatigue

crack growth based on the Williams' series. International Journal of Solids and Structures 53, 38–47. URL: https://linkinghub.elsevier.com/retrieve/pii/S0020768314004053, doi:10.1016/j.ijsolstr.2014.10.026.

Réthoré, J., 2015. Automatic crack tip detection and stress intensity factors estimation of curved cracks from digital images: Automatic crack tip detection and SIF estimation of curved cracks. Int. J. Numer. Meth. Engng 103, 516–534. URL: https://onlinelibrary.wiley.com/doi/10.1002/nme.4905, doi:10.1002/nme.4905.

Réthoré, J., 2018. UFreckles. URL: https://zenodo.org/record/1433776, doi:10.5281/ZENODO.1433776. language: en.

Réthoré, J., Estevez, R., 2013. Identification of a cohesive zone model from digital images at the micron-scale. Journal of the Mechanics and Physics of Solids 61, 1407–1420. URL: https://linkinghub.elsevier.com/retrieve/pii/S0022509613000288, doi:10.1016/j.jmps.2013.01.011.

Réthoré, J., Roux, S., Hild, F., 2011. Optimal and noise-robust extraction of Fracture Mechanics parameters from kinematic measurements. Engineering Fracture Mechanics 78, 1827–1845. URL: https://linkinghub.elsevier.com/retrieve/pii/S0013794411000312, doi:10.1016/j.engfracmech.2011.01.012.

Sagar, R.V., Prasad, B.R., Kumar, S.S., 2012. An experimental study on cracking evolution in concrete and cement mortar by the b-value analysis of acoustic emission technique. Cement and Concrete Research 42, 1094–1104. URL: https://linkinghub.elsevier.com/retrieve/pii/S0008884612000981, doi:10.1016/j.cemconres.2012.05.003.

Schau, H., Robinson, A., 1987. Passive source localization employing intersecting spherical surfaces from time-of-arrival differences. IEEE Trans. Acoust., Speech, Signal Process. 35, 1223–1225. URL: http://ieeexplore.ieee.org/document/1165266/, doi:10.1109/TASSP.1987.1165266.

Schmidt, R.O., 1972. A New Approach to Geometry of Range Difference Location. IEEE Trans. Aerosp. Electron. Syst. AES-8, 821–835. URL: http://ieeexplore.ieee.org/document/4103057/, doi:10.1109/TAES.1972.309614.

Scruby, C.B., 1987. An introduction to acoustic emission. J. Phys. E: Sci. Instrum. 20, 946–953. URL: https://iopscience.iop.org/article/10.1088/0022-3735/20/8/001, doi:10.1088/0022-3735/20/8/001.

Sung, D.U., Oh, J.H., Kim, C.G., Hong, C.S., 2000. Impact Monitoring of Smart Composite Laminates Using Neural Network and Wavelet Analysis. Journal of Intelligent Material Systems and Structures 11, 180–190. URL: http://journals.sagepub.com/doi/10.1106/N5E7-M37Y-3MAR-2KFH, doi:10.1106/N5E7-M37Y-3MAR-2KFH.

Vasudevan, A.V., 2018. Deciphering triangular fracture patterns in PMMA : how crack fragments in mixed mode loading. Ph.D. thesis. Sorbonne University. URL: https://tel.archives-ouvertes.fr/tel-02180510.

Vincent-Dospital, T., Toussaint, R., Santucci, S., Vanel, L., Bonamy, D., Hattali, L., Cochard, A., Flekkøy, E.G., Måløy, K.J., 2020. How heat controls fracture: the thermodynamics of creeping and avalanching cracks. Soft Matter 16, 9590–9602. URL: http://xlink.rsc.org/?DOI=D0SM01062F, doi:10.1039/D0SM01062F.

Vinel, A., Seghir, R., Berthe, J., Portemont, G., Réthoré, J., 2021. Metrological assessment of multi-sensor camera technology for spatially-resolved ultra-high-speed imaging of transient high strain-rate deformation processes. Strain 57. URL: https://onlinelibrary.wiley.com/doi/10.1111/str.12381, doi:10.1111/str.12381.

Wadley, H., Mehrabian, R., 1984. Acoustic emission for materials processing: a review. Materials Science and Engineering 65, 245–263. URL: https://linkinghub.elsevier.com/retrieve/pii/0025541684900867, doi:10.1016/0025-5416(84)90086-7.

Wang, B., Zhong, S., Lee, T.L., Fancey, K.S., Mi, J., 2020. Non-destructive testing and evaluation of composite materials/structures: A state-of-the-art review. Advances in Mechanical Engineering 12, 168781402091376. URL: http://journals.sagepub.com/doi/10.1177/1687814020913761, doi:10.1177/1687814020913761.

Williams, M.L., 1957. On the Stress Distribution at the Base of a Stationary Crack. Journal of Applied Mechanics 24, 109–114. URL: https://asmedigitalcollection.asme.org/appliedmechanics/article/24/1/109/1110895/On-the-Stress-Distribution-at-the-Base-of-a, doi:10.1115/1.4011454.

Zhou, Z., Lan, R., Rui, Y., Dong, L., Cai, X., 2021. A New Algebraic Solution for Acoustic Emission Source Localization without Premeasuring Wave Velocity. Sensors 21, 459. URL: https://www.mdpi.com/1424-8220/21/2/459, doi:10.3390/s21020459.

Zhou, Z., Rui, Y., Zhou, J., Dong, L., Cai, X., 2018. Locating an Acoustic Emission Source in Multilayered Media Based on the Refraction Path Method. IEEE Access 6, 25090–25099. URL: https://ieeexplore.ieee.org/document/8290682/, doi:10.1109/ACCESS.2018.2805384.